

# Science Using Single-Pulse Exploration with Combined Telescopes (SUSPECT)

## I. The mode-switching, flaring, and single-pulse morphology of PSR B1822–09

F. Jankowski<sup>1\*</sup>, J.-M. Grießmeier<sup>1,2</sup>, M. Surnis<sup>3</sup>, G. Theureau<sup>1,2,4</sup>, and J. Pétri<sup>5</sup>

<sup>1</sup> LPC2E, Université d'Orléans, CNRS, 3A Avenue de la Recherche Scientifique, 45071 Orléans, France  
e-mail: fabian.jankowski@cnrs-orleans.fr

<sup>2</sup> Observatoire Radioastronomique de Nançay, Observatoire de Paris, Université PSL, Université d'Orléans, CNRS, 18330 Nançay, France

<sup>3</sup> Department of Physics, IISER Bhopal, Bhauri Bypass Road, Bhopal, 462066, India

<sup>4</sup> LUTH, Observatoire de Paris, Université PSL, Université Paris Cité, CNRS, 92195 Meudon, France

<sup>5</sup> Université de Strasbourg, CNRS, Observatoire astronomique de Strasbourg, UMR 7550, F-67000 Strasbourg, France

Received XXX; accepted XXX

### ABSTRACT

*Context.* Radio pulsars exhibit a plethora of complex phenomena at the single-pulse level. However, the intricacies of their radio emission remain poorly understood.

*Aims.* We aim to elucidate the pulsar radio emission by studying several single-pulse phenomena, how they relate to each other, and how they evolve with observing frequency. We intend to inspire models for the pulsar radio emission and fast radio bursts.

*Methods.* We set up an observing programme called the SUSPECT project running at the Nançay Radio Observatory telescopes in France (10 – 85 MHz, 110 – 240 MHz, 1 – 3.5 GHz) and the upgraded Giant Metrewave Radio Telescope (uGMRT) in India. In this first paper, we focus on high-sensitivity data obtained of PSR B1822–09 with the uGMRT between 550 and 750 MHz. The pulsar has precursor (PC), main pulse (MP), and interpulse (IP) emission, and exhibits mode-switching. We present its single-pulse stacks, investigate its mode-switching using a hidden Markov switching model, and analyse its single-pulse morphology.

*Results.* PSR B1822–09's pulse profile decomposes into seven components. We show that its mode-switching is well described using a hidden Markov switching model. The pulsar exhibits at least three stable emission modes, one of which is a newly discovered bright flaring mode. We confirm that the PC and MP switch synchronously to each other, and both asynchronously to the IP, indicating information transfer between the polar caps. Additionally, we performed a fluctuation spectral analysis and discovered three fluctuation features in its quiescent Q-mode emission, one of which is well known. We conclude that it is longitude-stationary amplitude modulation. Finally, we visually classified the single-pulses into four categories. We found extensive 0.2 – 0.4 ms microstructure in the PC with a typical quasi-periodicity of 0.8 ms. There is low-level PC activity during the Q-mode, indicating mode mixing. We discovered low-intensity square-like pulses and extremely bright pulses in the MP, which suggest bursting.

*Conclusions.* PSR B1822–09's PC resembles magnetar radio emission, while its MP and IP are canonical radio pulsar like. Hence, the pulsar combines both attributes, which is rare in the known population. We introduced several new data analysis techniques to pulsar astrophysics.

**Key words.** pulsars: general – pulsars: individual: B1822-09 – methods: data analysis – radiation mechanisms: non-thermal – techniques: interferometric

## 1. Introduction

The vast majority of radio pulsars exhibit pulse profiles that are stable in time when thousands of their individual pulses are averaged. However, a small number of pulsars are known to switch between two or more stable emission modes with distinct pulse profiles. This phenomenon is commonly known as mode-switching (Backer 1970c). The switching between the emission modes can happen quasi-randomly and is in at least some cases correlated with changes in the spin-down rate  $\dot{\nu}$  of the neutron star (Lyne et al. 2010). A closely related phenomenon is the apparent cessation of radio emission from a pulsar, known as nulling (Backer 1970d; Biggs 1992; Wang et al. 2007). More extreme cases of this exhibit the so-called long-term intermit-

tent pulsars that routinely turn off for weeks to years (Kramer et al. 2006; Lyne et al. 2017). Other pulsars show systematic and recurring shifts of their single-pulse profiles in phase from rotation to rotation, known as drifting sub-pulses (Weltevrede et al. 2006; Song et al. 2023). While drifting sub-pulses seem to be relatively common in the pulsar population (Backer 1973; Weltevrede et al. 2006; Song et al. 2023), nulling, mode-changing, and long-term intermittency seem to be much rarer phenomena (Fowler et al. 1981). The list above is ordered by decreasing relative occurrence, which in turn is influenced by observational bias from insufficient monitoring of large pulsar samples. In any case, the fact that only a small number of pulsars (a few percent of the current population) are known to exhibit mode-switching and other related phenomena makes them attractive exceptional cases. We argue that they provide essential clues to understanding the physical properties and effects in the highly-magnetised

\* Corresponding author.

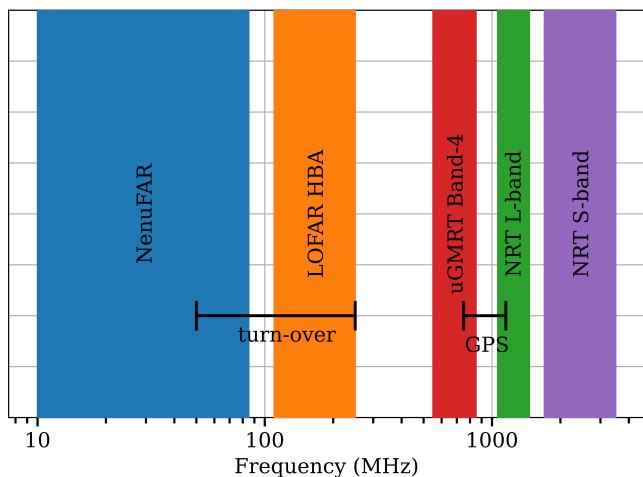


**Fig. 1.** Schematic overview illustrating the frequency coverage of our data from the Nançay Radio Observatory telescopes (NenuFAR, LOFAR FR606, and NRT) together with the uGMRT Band-4 data. We also show the typical frequency ranges of low-frequency turn-overs in pulsar radio spectra and the peak frequencies of gigahertz-peaked spectrum (GPS) pulsars for reference.

plasma that fills pulsar magnetospheres and the radio emission mechanism.

### 1.1. The Science Using Single-Pulse Exploration with Combined Telescopes (SUSPECT) project

We devised an observing project called “Science Using Single-Pulse Exploration with Combined Telescopes” (SUSPECT) to understand better several pulsar single-pulse phenomena. The acronym also encapsulated our focus on several of the “usual suspect” relatively bright radio pulsars to achieve the required high signal-to-noise ratio (S/N) per pulse. The words “combined telescopes” indicate that we acquire most of our data using multi-element radio interferometers and that we aim for simultaneous observations. Our primary objectives are to (1) measure and analyse the frequency dependence of pulsar single-pulse properties, such as mode-switching, nulling, and sub-pulse drifting. (2) Secondly, we focus on exotic single-pulse behaviour, such as flaring, bursting, or “swooshing” (Rankin et al. 2006; Wahl et al. 2016; Basu et al. 2021). (3) Another motivation is to relate our pulsar single-pulse measurements with fast radio burst (FRB) phenomenology as observed, for instance, in repeating FRBs. We aim to inspire models for the FRB emission based on the plasma physics processes happening in pulsar magnetospheres, which themselves are not fully understood. More traditional objectives are (4) to study the evolution of the pulsars’ integrated pulse profiles with frequency and to distinguish between propagation and intrinsic effects, such as the radius-to-frequency mapping model (Cordes 1978). In this paradigm, the radio emission observed at different frequencies is believed to originate from different altitudes in the pulsar’s magnetosphere. (5) The simultaneous wide frequency coverage of the data naturally allows us to measure the pulsars’ radio spectra with high accuracy. A solid tie to the absolute flux density scale of the primary (gain, phase, and flux) calibrator from synthesis imaging is incredibly beneficial.

It is crucial to obtain pulsar measurements over a wide frequency range, ideally truly simultaneously, to study the objec-

tives above. This is to eliminate the effect of temporal changes in the pulsar intrinsic emission process and any propagation effects in the interstellar medium. Rotation-simultaneous data ensure that the telescopes’ observing frequency is the only variable, that the pulsar was in exactly same emission state, and the interstellar medium almost unchanged<sup>1</sup>. In practice, we achieved this by observing our pulsar sample simultaneously with several telescopes at the Nançay Radio Observatory in France, each covering a distinct but highly complementary frequency range. For additional frequency coverage, we observed with the upgraded Giant Metrewave Radio Telescope (uGMRT) in India. As shown schematically in Fig. 1, we use NenuFAR (10 – 85 MHz), the French LOFAR station FR606’s HBA antennas (110 – 240 MHz), the uGMRT in Band-4 (550 – 750 MHz), and the Nançay Radio Telescope (NRT) at 1.0 – 1.8 and 1.7 – 3.5 GHz for this project. In the future, we might extend the project to other facilities.

### 1.2. The pulsar B1822–09

PSR B1822–09 (PSR J1825–0935) was discovered in the Jodrell Bank A pulsar survey at 408 MHz (Davies et al. 1972) and is an interesting pulsar that exhibits a wealth of peculiar phenomena. It is one of the rare pulsars with interpulse emission separated by about half a turn from the main pulse and most likely coming from the opposite pole of the star (Hermsen et al. 2017). Moreover, it shows mode-switching, sub-pulse drifting (Fowler et al. 1981), spin-up glitches with strange recoveries (Shabanova 2007; Yuan et al. 2010), and correlated profile and spin-down rate changes (Lyne et al. 2010). It is a relatively young 769-ms period radio pulsar with an unusually high period derivative of  $5.24 \times 10^{-14} \text{ ss}^{-1}$  (Jankowski et al. 2019). It has a dispersion measure of  $19.3833 \text{ pc cm}^{-3}$  (Stovall et al. 2015), which places it at a DM-inferred distance of 262 pc, according to the ymw16 Galactic free-electron model (Yao et al. 2017). Additionally, based on an HI emission/absorption distance limit, its Lutz-Kelker bias corrected distance is  $0.3^{+0.7}_{-0.2} \text{ kpc}$  (Verbiest et al. 2012). It has a characteristic age of 233 kyr, a spin-down luminosity of  $4.5 \times 10^{33} \text{ erg s}^{-1}$ , and a surface dipole magnetic field strength of  $6.42 \times 10^{12} \text{ G}$ . The pulsar is reasonably bright in the radio band with a mode-averaged flux density of 24 mJy at 843 MHz (Jankowski et al. 2019) and 10 mJy at 1.4 GHz (Johnston & Kerr 2018). Its radio spectrum is highly complex (Gil et al. 1994), with published detections down to 42 MHz (Suleymanova et al. 2012) and below 40 MHz with NenuFAR. An associated X-ray counterpart was identified (Prinz & Becker 2015) and its sinusoidal pulsed emission was unambiguously detected (Hermsen et al. 2017). Gamma-ray counterparts were suggested early on (Pinkau 1979; Mandrou et al. 1980) and Hermsen et al. (2017) presented a marginal detection of the pulsar’s emission in GeV  $\gamma$ -rays based on *Fermi* satellite data. However, the pulsar is absent in the third *Fermi* Large Area Telescope Pulsar Catalogue (Smith et al. 2023).

PSR B1822–09 is a well known mode-changing pulsar that exhibits classical mode-switching with two distinct emission modes. Its radio pulse profile consists of a main pulse (MP), a precursor (PC), and an interpulse (IP) profile component (Fowler et al. 1981; Morris et al. 1981). It has a relatively stable and long-lasting quiescent mode (Q-mode) of typically 4.5-min duration that is present about 64 per cent of the time. It gets interrupted by a significantly brighter burst mode (B-mode) that

<sup>1</sup> To a good first order. However, the Earth’s ionosphere induces location-dependent effects that must ideally be compensated.

is short-lived and typically lasts only 2.5 min (Fowler et al. 1981; Hermsen et al. 2017). The B-mode is characterised by the appearance of the PC component about 15 deg before to the MP, which is absent or extremely weak in the Q-mode. The MP consists of two sub-components with a characteristic shoulder (Fowler et al. 1981; Gil et al. 1994). The pulsar exhibits mode-dependent sub-pulse drifting and modulation. During the Q-mode, the MP and IP show a long-period modulation with a periodicity  $P_3 = 40 - 47 P_1$ , where  $P_1$  is the pulsar’s rotation period. This was initially thought to be caused by sub-pulse drifting (Fowler et al. 1981), but seems to be due to longitude-stationary intensity modulation of unknown physical origin (Gil et al. 1994; Yan et al. 2019), or a mixture of amplitude and phase amplitude modulation (Backus et al. 2010; Latham et al. 2012). In the B-mode, the long-period modulation ceases and only short sequences of pulses with a much faster drift rate of  $P_3 \approx 11 P_1$  were reported (Fowler et al. 1981; Gil et al. 1994). In data obtained at 325 MHz, Latham et al. (2012) reported a modulation of  $P_3 = 70 P_1$ . Interestingly, the PC component appears to have an almost flat spectral index, which is significantly different from that of the MP (Fowler et al. 1981; Gil et al. 1994). The PC is almost 100 per cent linearly polarised and shows a flat polarisation position angle reminiscent of the Crab pulsar’s precursor, which has a very steep radio spectrum (Manchester et al. 1980; Johnston & Kerr 2018). Despite the detection of pulsed X-ray emission from the pulsar, no evidence was found for simultaneous mode-switching between its X-ray and radio emission (Hermsen et al. 2017), which is in contrast to what has been discovered for other mode-switching radio and X-ray pulsars, although the sample size is tiny (3; Hermsen et al. 2018). Moreover, PSR B1822–09 is one of the few pulsars for which Lyne et al. (2010) found a significant correlation between its profile shape and spin-down rate. The ratio of its PC and MP amplitudes correlates positively with its spin-down rate on  $\sim 10$  yr timescales (Lyne et al. 2010).

Inferring a pulsar’s true geometry is challenging, but the most prevalent belief is that PSR B1822–09 is an almost orthogonal rotator and that the PC and MP on one hand and the IP on the other come from opposing magnetic poles of the star (Hankins & Fowler 1986; Gil et al. 1994; Backus et al. 2010; Hermsen et al. 2017). Curiously, the IP participates in the mode-switching, where it switches intensity asynchronously with the PC and synchronously with the MP (Gil et al. 1994). This phase-locked relationship between the emission from both poles of the star strongly suggests an information transfer between the radio emission regions at opposite poles, which is unexpected and challenging to explain physically (Fowler et al. 1981; Fowler & Wright 1982; Gil et al. 1994). Dyks et al. (2005) suggested a somewhat unorthodox model in which a single radiation source creates both the PC and IP. They proposed that the IP originates because of a 180 degree flip in emission direction of the source inwards, i.e. towards the star.

PSR B1822–09’s rotation gets regularly interrupted by spin-up glitches with 14 events currently listed in the Australia Telescope National Facility pulsar catalogue (Manchester et al. 2005). Several of them are so-called slow glitches with unusual signatures that consist of sharp increases in spin-down rate  $\dot{\nu}$  that relax quasi-exponentially to their pre-glitch values over hundreds of days (Shabanova 2007; Yuan et al. 2010; Lyne et al. 2010). The two strongest  $\dot{\nu}$  events appear positively correlated with the pulse shape, namely the PC to MP amplitude ratio (Lyne et al. 2010). That is, the amplitude ratio PC / MP increased during episodes of increased  $\dot{\nu}$ . Interestingly, there is some evidence

that its integrated pulse profile in both emission modes changed subtly after two glitches of normal signature (Liu et al. 2022).

In Sec. 2, we describe our observations and the data reduction performed. In Sec. 3, we present the pulsar’s single-pulse stacks, our model for its mode-switching process, mode-separated profiles, and a detailed analysis of its single-pulse morphology. In Sec. 4, we discuss our results and compare them with measurements from the literature. Finally, we present our conclusions in Sec. 5.

## 2. Observations and data processing

As part of the uGMRT project “Understanding the wide-band single-pulse properties of bright radio pulsars with the upgraded GMRT” (44\_056 and 45\_029, PI: Jankowski), we obtained beamformed high time-resolution data of PSR B1822–09 at Band-4 frequencies. Starting from UT 2023-04-24 22:22, we recorded  $2 \times 56$  min of total intensity (Stokes I) data in two pointings separated by a phase calibrator scan of 6 min. On UT 2023-12-05 11:40, we observed the pulsar for 45 and 37 min again separated by a 6 min calibrator scan. The data were obtained between 550 – 750 MHz with 200 MHz of digitised bandwidth. We used the GMRT Wideband Backend (GWB) to record 2048 frequency channels at a sampling time of 81.92  $\mu$ s. Both 8-bit phased-array (PA) and 16-bit data coherently dedispersed (CD) at the pulsar’s catalogued DM of 19.3833 pc cm<sup>-3</sup> (Stovall et al. 2015) were saved. However, the fine channelisation ( $\sim 97.66$  kHz channel bandwidth) alone was sufficient to reduce the intra-channel dispersive smearing to just above one time sample at 550 MHz and below half a sample at 750 MHz. On 2023-12-05, we saved post-correlation mode data instead of the CD data. The signals from 16 – 17 GMRT antennas were combined in phase, allowing for high sensitivity. Tab. 1 summarises the properties of our observational data.

After obtaining the raw data, we used the `RFICLEAN` software (Maan et al. 2021) to convert them to `SIGPROC` filterbank files (Lorimer 2011) and perform an initial step of radio frequency interference (RFI) excision. `RFICLEAN` excised periodic (e.g. mains power) and impulsive RFI. We then employed the `DSPSR` software (van Straten & Bailes 2011) to create dedispersed single-pulse files with 4096 phase bin resolution (187.74  $\mu$ s) based on the best available pulsar ephemeris. Some further manual RFI excision and standard post-processing tasks were performed using the `PSRCHIVE` software suite (Hotan et al. 2004). We subtracted the profile baselines using the `PSRSALSA` software (Weltevrede 2016). Additionally, we updated the pulsar’s period in the ephemeris and verified it using standard pulsar timing techniques via the `TEMPO2` software (Hobbs et al. 2006). The observations were phase aligned by rotating the 2023-12-05 data by  $\sim 0.282$  in phase with respect to the 2023-04-24 data, as determined from the timing fit. The data currently lack a robust absolute flux density calibration. For all further data analysis we used a custom `PYTHON`-based software suite called `SPANALYSIS` in version 0.4.4 that we developed for single-pulse analysis tasks.

## 3. Results

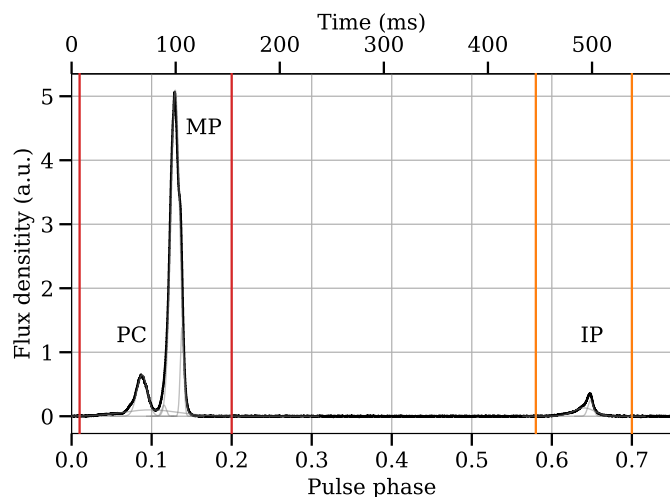
### 3.1. Total integrated pulse profile, profile components, and single-pulse stacks

Fig. 2 shows the pulsar’s total integrated pulse profile formed from the 2023-04-24 data with the different profile features clearly visible. Its integrated profile consist of a main pulse and interpulse on-pulse phase regions, delineated by the vertical red



**Table 1.** Details of the uGMRT data presented in this work. We list the observing date, the start UT, the observing time  $t_{\text{obs}}$ , the centre frequency  $\nu_c$ , the digitised bandwidth  $b$ , the number of frequency channels  $N_{\text{chan}}$ , the sampling time  $t_{\text{samp}}$ , the number of antennas included in the imaging  $N_{\text{ant,im}}$  and phased array  $N_{\text{ant,pa}}$  data streams, and the number of pulsar single-pulses recorded  $N_{\text{pulse}}$ .

Date (yyyy-mm-dd)	Start (UT) (hh:mm)	$t_{\text{obs}}$ (min)	$\nu_c$ (MHz)	$b$ (MHz)	$N_{\text{chan}}$	$t_{\text{samp}}$ ( $\mu\text{s}$ )	$N_{\text{ant,im}}$	$N_{\text{ant,pa}}$	$N_{\text{pulse}}$
2023-04-24	22:22	56 + 56	650	200	2048	81.92	29	16	8,743
2023-12-05	11:40	45 + 37	650	200	2048	81.92	28	16	6,362
Total	–	194	–	–	–	–	–	–	15,105



**Fig. 2.** Total integrated pulse profile of PSR B1822–09 formed from our 2023-04-24 data that shows its precursor (PC), main pulse (MP), and interpulse (IP) profile components. The IP is separated by about 0.52 in phase from the MP. The coloured vertical solid lines delineate the two on-pulse phase ranges and the grey solid lines show our best decomposition into seven von Mises distribution sub-components.

and orange lines that we placed visually. The main pulse region contains the precursor (PC) and the main pulse (MP) profile components. The interpulse (IP) is separated from the MP by about half a rotation of the star ( $\sim 0.52$  phase peak-to-peak), which likely makes it a genuine IP, i.e. emission from the polar cap on the opposite side of the star. The grey solid lines in Fig. 2 show our best profile decomposition into scaled von Mises distribution sub-components

$$f(\varphi|\mu, \kappa) = A \exp \{ \kappa [\cos(\varphi - \mu) - 1] \}, \quad (1)$$

where  $\varphi \in [0, 2\pi]$  is the pulsar rotational phase,  $A$  the amplitude,  $\mu$  the mean, and  $\kappa$  the concentration, i.e. the inverse of the Gaussian variance. The definition above is slightly adjusted from its standard form for numerical convenience and compatibility with the implementation in `PSRCHIVE`. In this model, the profile consists of seven sub-components in total, two in the PC, four in the MP, and two in the IP, where one component spans both the PC and MP. In particular, the PC consists of a bright primary sub-component in the centre and a significantly fainter and wider plateau component, which also contributes to the bridge emission and the MP. The MP is complex with a strong primary sub-component on the leading side, a somewhat fainter trailing shoulder component, and a tiny bump at the leading edge. The IP is made up of a narrow bright component at the trailing edge and a wider and fainter component at the leading side that is responsible for the IP’s asymmetry. The PC has roughly 13 per cent of the peak flux of the MP, and the IP 7 per cent. Integrating across the profile components, we find that the MP carries about

79 per cent of the total pulse-averaged flux density. The PC and IP contribute 14 and 7 per cent to the mode-averaged total. It is interesting that the PC is almost exactly twice as bright as the IP in both the peak and pulse-averaged sense in this frequency band, which could point to a common origin, as was suggested earlier (Dyks et al. 2005).

We present the single-pulse stacks for the 2023-04-24 observation in Fig. 3. The left panel shows the first 56 min of data and the right panel the second, with a gap of 6 min in between. Fig. 4 shows the same, but for the observation on 2023-12-05. In both figures, we zoomed in slightly in pulse phase for clarity. The bottom panels show the normalised mean pulse profile computed over that pulse stack as black solid lines referenced to the left amplitude  $A$  scale and the phase-resolved time-domain modulation index

$$m_i = \frac{\sigma_i}{\mu_i} \quad (2)$$

with black error bars referenced to the right modulation  $m$  scale, where  $\sigma_i$  is the standard deviation and  $\mu_i$  the mean Stokes I profile intensity at the phase bin  $i$ . We show the modulation index only for phase bins where the mean profile exceeds 1 or 2 per cent of its peak amplitude and estimated its uncertainties robustly by bootstrap resampling the data 100 times. The on and off switching of the PC component is clearly visible. The switching time was significantly shorter (more frequent) in the first 2023-04-24 scan compared with the second. The pulsar switched into its B-mode nine times during that observation. The switching was slightly less frequent in the 2023-12-05 data, where the pulsar was in the B-mode seven times. The phase-resolved modulation index is qualitatively similar in each of the four scans. The most stable emission (lowest  $m_i$ ) originates near the centre of the MP, approximately aligned with the hump in the profile. The MP’s leading edge has a slightly higher modulation with a small S-shaped bump visible in the  $m_i$  curve. The modulation index increases across the bridge between the MP and PC until it decreases again in the PC phase range where it reaches another local minimum. The modulation index there is several times higher than in the MP and is dominated by the mode-switching process. The modulation index increases roughly symmetrically at the profile edges, as expected. The IP shows a V-like  $m_i$  curve that is practically featureless but slight asymmetric towards its leading profile edge, tracing its profile shape. The minimum occurs near the IP’s profile peak. We analyse the pulsar’s switching behaviour in detail in the following sections.

### 3.2. Understanding the pulsar’s mode-switching

The first step in any mode-switching pulsar analysis is to determine how many different stable emission modes a pulsar exhibits and to separate them in the pulse stacks. This mode classification or sequencing is a crucial first step for any following analyses and thus greatly influences any conclusions drawn. This is



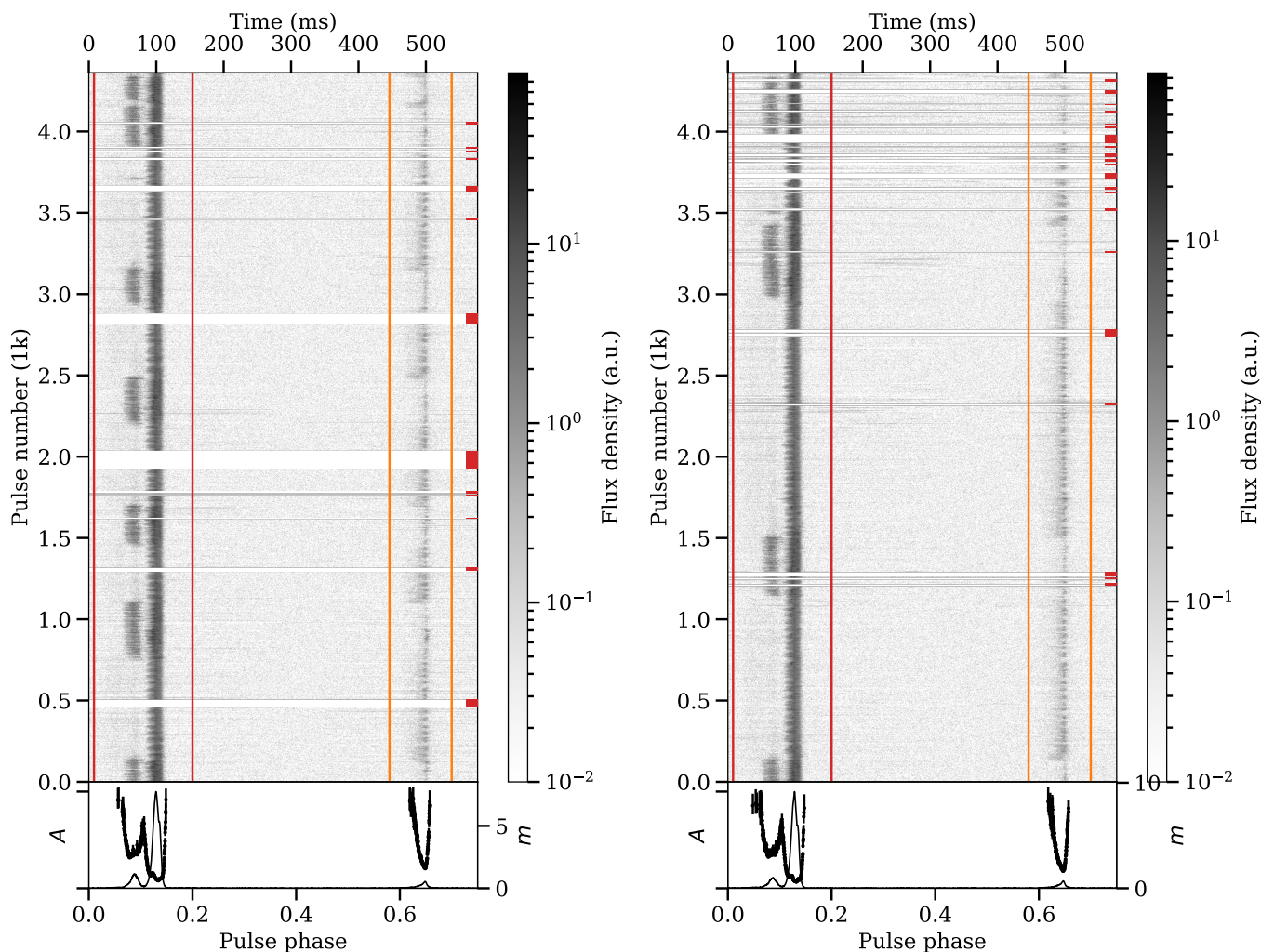


**Fig. 3.** Single-pulse stacks of PSR B1822–09 from our data taken on 2023-04-24 showing several mode transitions. Each stack contains 56 min of data with a gap of 6 min between them for the phase calibrator scan. We applied a logarithmic greyscale mapping to bring out the faint emission in the IP and around the mode transitions. The vertical coloured lines delimit the two on-pulse phase regions and the horizontal red lines on the right mark the rotations that were excised. The bottom panels show the normalised mean profile amplitudes  $A$  (black solid lines; left scale) and the phase-resolved modulation index  $m$  (black error bars; right scale).

usually done visually from the pulse stacks or by looking at the intensity of emission in distinct pulse phase windows, where in the case of PSR B1822–09 the presence of its PC is taken as the mode determining feature (Fowler et al. 1981; Morris et al. 1981; Gil et al. 1994; Backus et al. 2010). The mode classification using the latter method can be performed quasi-automatically (Hermsen et al. 2017; Yan et al. 2019). However, it assumes that the pulsar emits in a single mode at a given time, i.e. it is a binary classification. In contrast, Latham et al. (2012) found evidence of mode mixing in PSR B1822–09 in the form of short emission sequences during which it was apparently emitting simultaneously in both modes. A different classification method is to decompose the single-pulse profiles into their Eigen mode profiles and analyse their mixture weights as a function of pulse number (Cao et al. 2023), which naturally incorporates mode mixing. Here, we describe a new mode classification method that uses time series of profile features as input.

### 3.2.1. A hidden Markov switching model for the pulsar’s moding process

With the aim of modelling the pulsar’s mode-switching we measured several features from the cleaned single-pulse stacks shown in Figs. 3 – 4. Among others, we measured rotation time series of the on-pulse fluence  $F_{\text{on}}$ , S/N, and boxcar equivalent pulse width  $W_{\text{eq}}$ . Additionally, we employed a peak-finding algorithm to determine the number of prominent  $S/N \geq 10$  pulse profile components or peaks  $N_p$  in the on-pulse region, their locations  $L_p$  in phase, and their full widths at half prominence  $W_p$ . In Fig. 5, we show an example single-pulse with the peaks and their full widths highlighted. Because of the S/N threshold,  $N_p$  is a robust lower limit for the actual number of peaked components in the profile. In particular, we confirmed that an additional small number of peaks were visible in the data close to the baseline noise limit, as is visible in Fig. 5. For each pulsar rotation we computed the median over all peak locations and widths as a summary statistic, which we denote as  $\text{med}(L_p)$  and  $\text{med}(W_p)$ , respectively. We show a comparison of the various feature time series in Fig. 6. We considered the combined PC and MP on-pulse phase range for this analysis, while the IP range was ex-

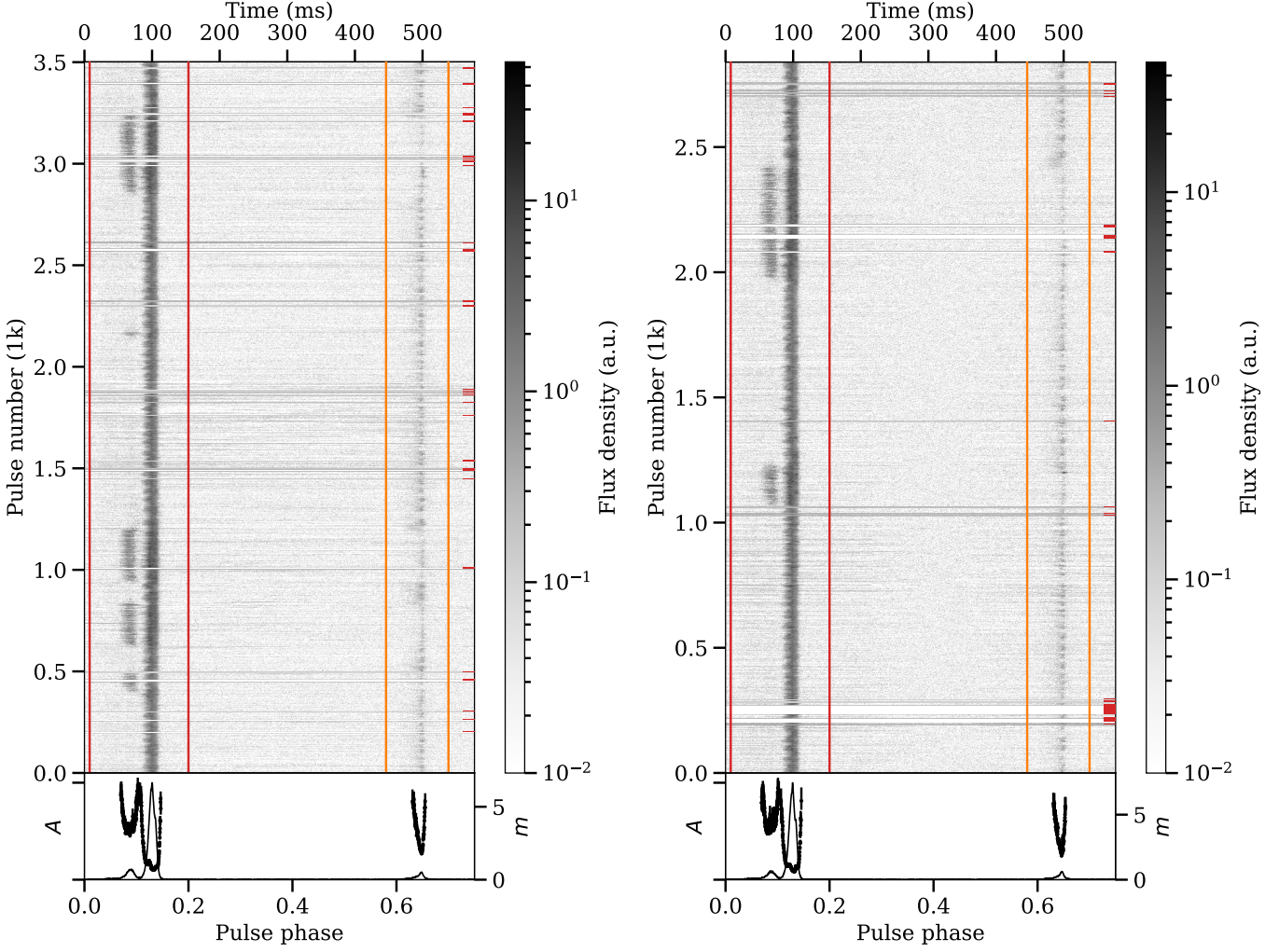


Fig. 4. Same as Fig. 3, but for the uGMRT data obtained on 2023-12-05.

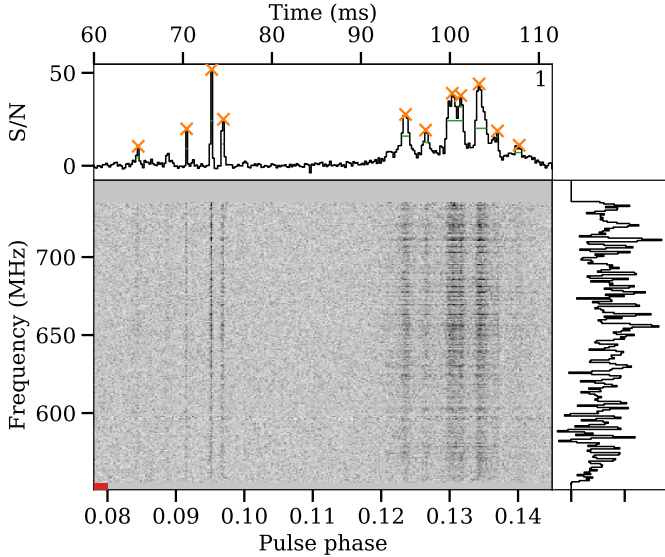
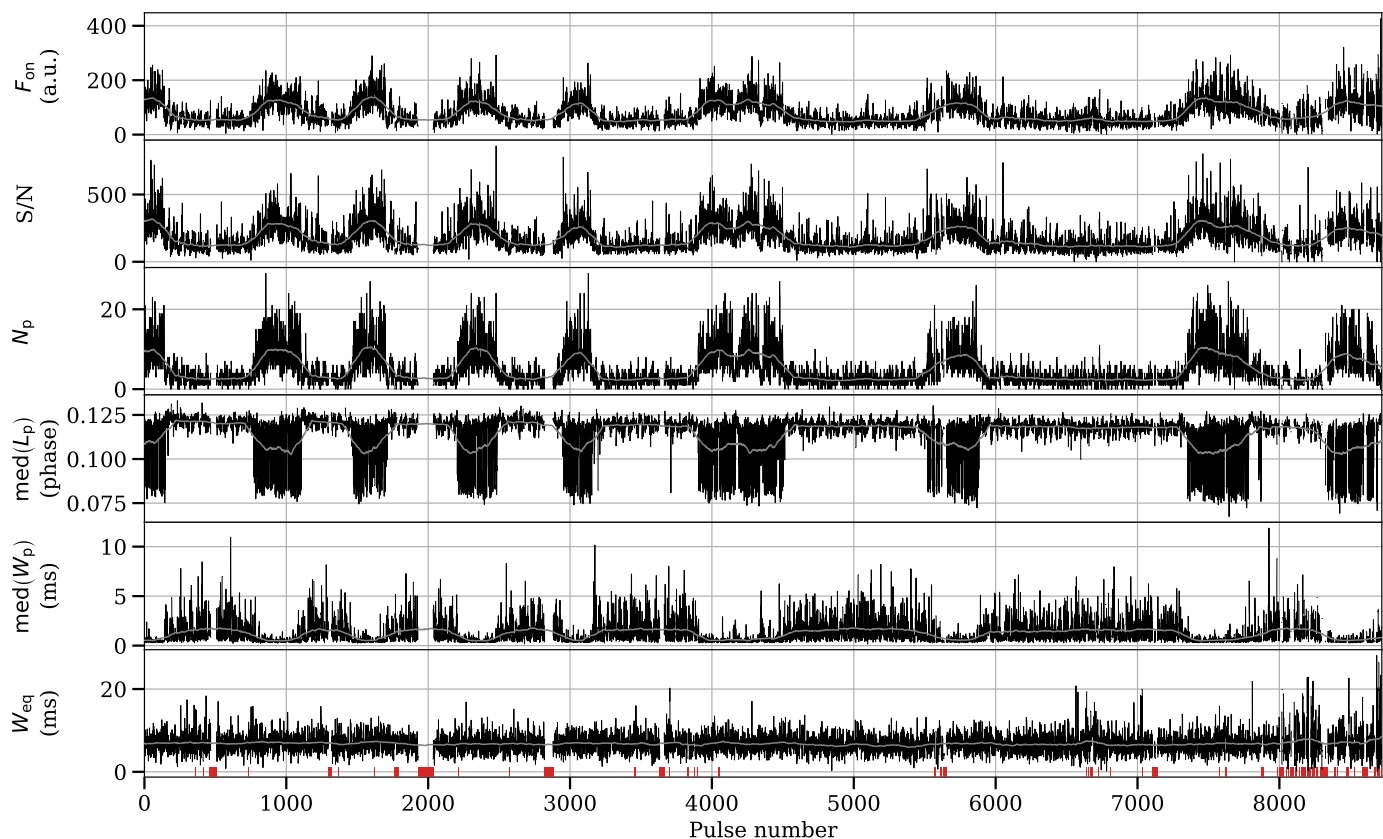


Fig. 5. Example of a single pulse dynamic spectrum and profile with the significantly peaked profile components and their full widths at half prominence highlighted. The right panel shows the mean power spectral density or radio spectrum in the on-pulse region. A sub-threshold peak is visible in the PC phase window on the left.

cluded. The mode-switching is clearly visible in the fluence, S/N,  $N_p$ ,  $L_p$ , and  $W_p$  series. The  $W_{eq}$  times series is too noisy at the single-pulse resolution. The fluence and S/N series beautifully reflect the doubling in pulse-averaged flux density when the pulsar switches from its Q- to its B-mode. The  $N_p$  and  $W_p$  time series in Fig. 6 nicely show the switching between single-pulses with a handful of peaked components of large width (Q-mode) and pulse profiles with 10–25 microshot-like components of extremely narrow width around one phase bin (B-mode). In other words, the  $N_p$  and  $W_p$  time series show alternating behaviour. The  $L_p$  time series nicely reflects the negative shift in median peak location due to the appearance of the PC profile component and its many peaks.

In a second step, we employed a hidden Markov model to describe the pulsar’s mode-switching process. It consists of two parts, (1) a model for the hidden transition process of the pulsar and (2) a model for the observed feature timelines for each hidden state. In particular, we modelled the pulsar as a stochastic system that exhibits  $N$  stable emission states  $S_t = \{0, 1, \dots, N-1\}$ . Those states are hidden or latent, i.e. not directly observable. We assumed that they obey the Markov property so that a given state  $S_t$  only depends on the state  $S_{t-1}$  directly before it. This way, the switching process can be described using a first-order Markov chain. The state transitions are represented





**Fig. 6.** Timeline showing several measured features from the entire 2023-04-24 single-pulse stack. Specifically, we show time series of the on-pulse fluence  $F_{\text{on}}$  in the combined PC and MP phase range, the S/N, the number of peaks  $N_p$  in the profile, their median locations  $L_p$  in pulse phase, their full widths at half prominence  $W_p$ , and the boxcar equivalent pulse width  $W_{\text{eq}}$ . The grey lines depict running mean smoothings of the data using a 150-rotation wide sliding window. The red vertical markers highlight rotations that were RFI excised.

using the  $N \times N$  square transition matrix

$$P(S_t|S_{t-1}) = [p_{ij}] = \begin{bmatrix} p_{00} & p_{10} & \cdots & p_{N-10} \\ p_{01} & p_{11} & \cdots & p_{N-11} \\ \vdots & \vdots & \ddots & \vdots \\ p_{0N-1} & p_{1N-1} & \cdots & p_{N-1N-1} \end{bmatrix}. \quad (3)$$

It describes the transition probability from state  $S_j$  (column) into the state  $S_i$  (row), i.e. it is read by looking at the column  $j$  first and the row  $i$  second. The off-diagonal elements  $p_{ij}, i \neq j$  describe the transition probabilities between states and the diagonal elements  $p_{ii}$  describe how stable a given state is in time (self-transition), where  $i, j \in \{0, 1, \dots, N-1\}$ . The matrix is left stochastic meaning that all columns must sum to unity,  $\sum_{j=0}^{N-1} p_{ij} = 1, \forall i$ . We then combined the hidden Markov model with a model for the observed feature time series for each stable pulsar emission state. Namely, we assumed that each state produced a measured time series  $y_t$  with a given mean  $\mu_{S_t}$ , a stochastic normally-distributed white-noise contribution  $\epsilon_{S_t} \sim N(0, \sigma_{S_t}^2)$ , where  $\sigma_{S_t}^2$  is the Gaussian variance, and further autoregressive terms that depend on the previous values  $y_{t-i}$  of the measured time series itself at the time lags  $i$ , which is analogue to recursion. Formally, this is given by

$$y_t = \mu_{S_t} + \epsilon_{S_t} + \sum_{i=1}^p \phi_i (y_{t-i} - \mu_{S_{t-1}}), \quad (4)$$

where  $p$  is the order of the autoregression and  $|\phi_i| < 1$  are the autoregression coefficients.  $\phi_i$  encode the transition behaviour of

the observed time series. While each hidden state  $S_t$  only depends on the previous  $S_{t-1}$ , the observed time series that is generated by the hidden states depend on the previously observed values of itself up to a given time lag  $p$ . More concretely,  $y_t$  can model decaying or oscillatory behaviour depending on the choice of  $\phi_i$ . Including the autoregressive terms in the model is important, as the measured feature time series show clear autoregressive behaviour. We verified this by computing their (partial) autocorrelation functions. For instance, the partial autocorrelation within the  $F_{\text{on}}$  and  $N_p$  time series stays significant until about lag 20 with a few non-negligible peaks beyond that. However, fitting an autoregressive switching model of that order is computationally challenging. Therefore, we limited ourselves to autoregressive orders  $p = 1-2$  and a global non-switching white noise term  $\epsilon_t$ . The combined model is called a hidden Markov switching autoregression model, which was originally developed for financial time series data in econometrics (Hamilton 1989, 2020). It is similar to a general mixture model combined with a temporal transition framework.

We then iteratively used each of the measured feature time series described above (Fig. 6) as input for our Markov switching model and estimated its free parameters using maximum likelihood regression via the expectation-maximisation algorithm. Based on the best-fitting parameters, we computed the marginalised probability time series  $p(S_t)$  of the pulsar being in state  $S_t$  at a given rotation, the average durations of each state, and the overall state fractions. The  $N_p$  time series had the highest mode-separation power at the single-pulse level out of the features that we tested. That is because the number of peaked profile



components is little affected by and therefore robust to the overall single-pulse brightness modulation above a limiting threshold peak S/N, which we set reasonably high (10 S/N). More importantly, the fact that the PC profile has a large number of peaked components makes  $N_p$  a reliable indicator for its activity. A less sensitive instrument will detect fewer peaked components, predominantly in the PC. The classification stays robust as long as the  $N_p$  distributions differ sufficiently between the modes. The above is true at the single-pulse level. However, the picture is likely different when rotation-integrated profiles are considered for the mode classification.

### 3.2.2. How many stable emission modes does the pulsar exhibit?

Using the Markov switching model described above, we investigated several questions. Firstly, we were interested in how many stable emission modes the pulsar exhibits. Apart from the two well-known ones (Q and B-mode) that are straightforward to identify visually, there could be additional more subtle modes hidden in the data. Or there could be mode mixing at certain times, as reported by Latham et al. (2012). We evaluated this question by successively increasing the number of states  $N$  of the Markov switching model, fitting it to the measured  $N_p$  feature time series data, and comparing the resulting residual plots and values of the Akaike information criterion (AIC; Akaike 1974) to prevent over-fitting. Specifically, we iteratively tested Markov switching models with  $N = 2 - 7$  states, a first order autoregressive term ( $p = 1$ ), and a globally constant (non-switching) white noise contribution (Eq. 4). A 2-state model is strongly disfavoured by the data in comparison with the other models tested. For all further analysis, we selected the 3-state model as the lowest-complexity model that describes the data well, with residuals that are almost white. Fig. 7 shows the diagnostic plot of our best-fitting 3-state model. The panels present from top to bottom: the  $N_p$  time series data, our best-fitting noise-free model, the model with additive Gaussian noise with the given best-determined global variance (M+N), the residual of the model plus noise (data - M+N), and the marginalised probability time series  $p(S_t)$  for each state. The bottom panel of Fig. 7 visualises the most-likely mode that was active during each pulsar rotation, where we used a different colour for each mode. Red corresponds to  $S_0$ , orange to  $S_1$ , and green to  $S_2$ . The best-fitting model parameters are  $\mu_0 = 2.68 \pm 0.04$ ,  $\mu_1 = 6.98 \pm 0.07$ ,  $\mu_2 = 15.8 \pm 0.1$ ,  $\sigma^2 = 3.75 \pm 0.06$ , and  $\phi_1 = 0.27 \pm 0.01$ . The fact that  $\phi_1$  deviates significantly from zero means that the time series shows clear autoregressive behaviour. The reduced  $\chi^2$  of the fit is 3.5 for 11 free model parameter and 8096 degrees of freedom. The best-fitting state transition matrix is

$$P(S_t|S_{t-1}) = \begin{bmatrix} >0.99 & 0.007 & 0.001 \\ 0.003 & 0.77 & 0.71 \\ <0.001 & 0.22 & 0.29 \end{bmatrix}. \quad (5)$$

The corresponding average state durations are 371.7, 4.2, and 1.3 rotations, or 285.9, 3.2, and 1 s, for  $S_0$  through  $S_2$ . The pulsar spent approximately 66, 26, and 8 per cent of the time in the different states. Fig. 8 visualises the transition probabilities between the modes in a Markov state diagram.  $S_0$  is a long-lived and stable dominant mode that is present for almost 70 per cent of the time. The number of profile peaks  $N_p$  is small around 3. There is a small probability of transitioning from  $S_0$  to  $S_1$ , whereas a direct transition from  $S_0$  to  $S_2$  is highly suppressed.  $S_1$  itself is relatively stable and is present in our data for about

**Table 2.** Component-resolved pulse-averaged flux density contributions for each of the emission modes. The percentages are affected by rounding.

Mode	Total (a.u.)	PC (%)	MP (%)	IP (%)
Q	0.09	6	81	10
B	0.15	17	80	3
Bf	0.21	34	63	2

25 per cent of the time. The typical number of peaks is higher ( $\sim 7$ ). The transition probability to  $S_2$  is considerable at around 20 per cent.  $S_2$  is an extremely transitory and short-lived mode with a large number of profile peaks ( $\sim 16$ ) present, which decays to  $S_1$  with around 70 per cent probability. It is active in our data for about 8 per cent of the time.

A somewhat independent way to investigate the number of emission modes and to verify our conclusions from the Markov switching model analysis is to look at histograms of the feature time series and try to decompose them into disjoint components belonging to each of the modes. We show examples of this in Fig. 9. The top panel shows a 1D histogram of the median peak location  $\text{med}(L_p)$ . The middle and bottom panels show scatter plots of two profile features against each other in what we call a feature space, with their 1D histograms at the sides. In the middle panel we show  $\text{med}(L_p)$  plotted against the total single-pulse S/N and in the bottom panel we show  $\text{med}(L_p)$  against the number of peaks  $N_p$ . In each case, the data reveal three obvious clusters in the  $\text{med}(L_p)$  domain, which corresponds to single-pulse profiles where the peaked profile components are dominant either in the PC (near 0.08 phase) or the MP (near 0.12 phase). The middle peak comes from single-pulses that have equal numbers of peaked profile components in the PC and MP phase ranges, which we denote as “equalised pulses”. Bridge emission with the MP inactive was not observed. More subtle clusters exist in the S/N domain, where the MP-dominated pulses have a most likely S/N around 100 (mode and contour), while the PC-dominated pulses cluster around 300 S/N. The equalised pulses seem to occupy the S/N range in between, near 200 S/N. The bottom panel of Fig. 9 gives the same picture for the  $N_p$  domain. The MP-dominated pulses cluster around 2 – 3 peaked profile components, the PC cluster is wide and centred at 12 – 13 peaks, and the equalised pulses cluster in the intermediate  $N_p$  range centred at 7. Thus, the visual histogram decomposition results in  $N_p$  centroid values that are very similar to the means from our Markov model analysis. In conclusion, the visual inspection of the feature histograms provides additional evidence that the pulsar exhibits at least three emission modes. We describe the profile morphology of each mode in the following section.

### 3.2.3. Mode-separated pulse profiles

Our next aims were to match the states identified by our Markov switching model to the physical emission modes of the pulsar, look at their mode-separated pulse profiles, and characterise them. To do that, we converted the most likely state membership time series shown in Fig. 7 bottom panel to binary selection masks, one for each state. We then applied the masks to the single-pulse stack data, selecting only the rotations that belonged to that particular state. Fig. 10 shows a comparison of the resulting mode-separated mean pulse profiles plotted on the same absolute scale. We show the combined PC and MP (left panel) and the IP phase range (right panel) separately for clarity. Emission

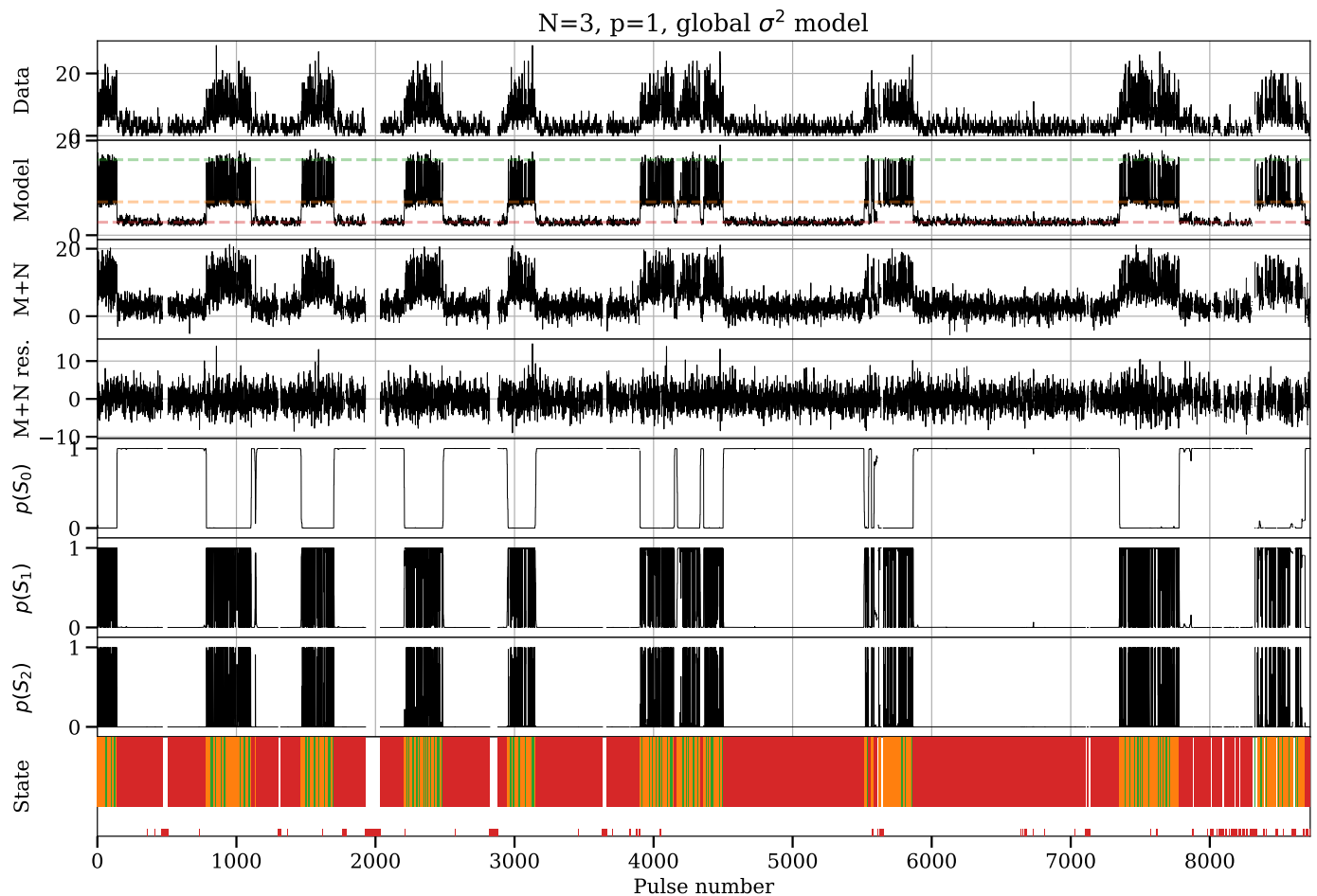


**Fig. 7.** Results from fitting our Markov switching models to our measured  $N_p$  time series data. We show the best fit of our 3-state model with first order autoregression and a globally constant variance. The panels show from top to bottom, the  $N_p$  time series data, the best-fitting noise-free switching model, the model with added Gaussian white noise with the estimated variance (M+N), the residuals of that (data - M+N), the state probability time series  $\rho(S_i)$ , and the most likely emission state for each rotation coloured separately. We show the best-fitting state means with dashed lines of the same colour in the model panel. As above, the red vertical markers highlight rotations that were RFI excised. The model describes the data well, with residuals that are almost white.

outside those phase windows was consistent with the baseline noise for all three states. Based on the appearance of their mode-separated pulse profiles, we identified state  $S_0$  as the quiescent Q-mode,  $S_1$  as the bright B-mode, and  $S_2$  as a newly discovered bright flaring Bf-mode. We describe each mode's characteristics in the following.

Considering the entire on-pulse window (PC, MP, and IP), the pulsar emitted continuously in each rotation that was unaffected by RFI, i.e. there was no evidence for nulling in our data. We show the measured total pulse-averaged flux densities and the component-resolved flux density fractions for each mode in Tab. 2. Namely, the PC, MP, and IP emission accounted for about 6, 81, and 10 per cent of the total emission in the Q-mode, roughly 17, 80, and 3 per cent in the B-mode, and approximately 34, 63, and 2 per cent in the Bf-mode.

The Q-mode is characterised by the PC being almost absent. Nonetheless, there is clearly detectable PC emission visible in the single-pulse stacks during some rotations that are otherwise pure Q-mode emission. This might be either caused by residual B/Bf-mode emission, i.e. the pulsar flickering into the B/Bf-mode for a few rotations, or genuine mode mixing, which we investigated in detail in Sec. 3.3.2. There is some small but measurable bridge emission between the PC and MP. The MP is

symmetric and almost triangular-shaped, except for the characteristic shoulder bump on the trailing edge. The IP is relatively bright (10 per cent of the total fluence) and strongly asymmetric with two kinks or bumps at the leading edge, which are likely caused by one or two additional emission sub-components, analogue to what we show in our von Mises profile decomposition in Fig. 2. The total flux density almost doubles ( $1.7\times$ ) when switching from the Q to the B-mode. However, this is not only because of the appearance of the PC profile component, the emission in the MP is also strongly enhanced. Specifically, the change is accounted for by a 70 per cent flux density increase in the MP, a  $5\times$  increase in the PC range, and a halving of the IP's flux density. The PC radiates much more intensely and a kink at its leading edge, reminiscent of a separate profile sub-component, is visible. The bridge emission increased slightly. The MP looks almost like a scaled up version of the Q-mode MP, except that the sub-component at the leading edge is enhanced, which results in a steepening of the leading profile edge and a slight shift of the profile maximum to earlier phases. The shoulder hump becomes more apparent. The IP emission is roughly halved, becomes more symmetric, and the central reference point on the peak shifts to slightly later phases. The trailing edge is little affected. The most prominent characteristic of the Bf-mode is

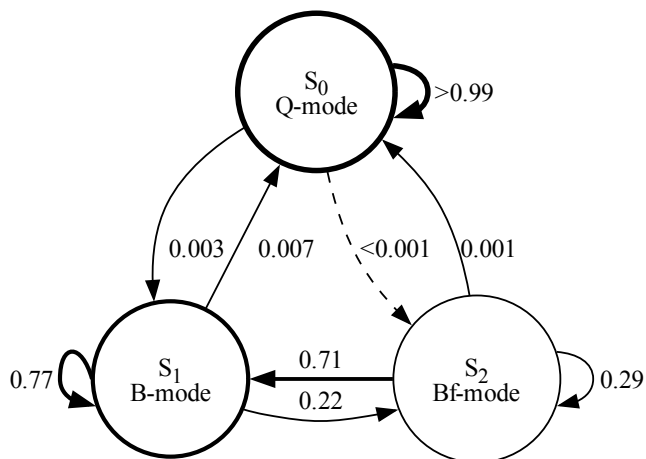


**Fig. 8.** Visualisation of the state transition probabilities of our best-fitting 3-state Markov switching model. The line thickness is roughly proportional to the transition probability, with low-probability transitions drawn using dashed lines. The identified states are the quiescent Q-mode, the bright B-mode, and a newly identified flaring Bf-mode.

that the amplitude or flux density ratio between the PC and MP is more equal at about 1:2. In other words, the PC contributes a significantly higher fraction of flux density than in the Q or B-modes. Indeed, the PC and MP look almost comparable in brightness in the single-pulse stacks. The kink in the PC becomes clearer and most of the additional emission comes from the centre of the PC envelope. The bridge emission near the PC’s trailing edge increased slightly. The brightness of the MP changes little and so does its shape. The IP is almost unchanged compared with the B-mode.

### 3.2.4. Fluctuation analysis

We performed a fluctuation analysis of the pulsar’s emission by computing a longitude-resolved fluctuation spectrum (LRFS; Backer 1970b,a, 1973) and a 2-dimensional fluctuation spectrum (2dFS; Edwards & Stappers 2002) of subsets of the single-pulse stacks. We first identified the longest continuous pulse number ranges during which the pulsar was emitting uninterrupted in one of its modes without switches, based on the single-pulse stacks shown in Figs. 3 – 4 and our Markov switching model classification above. For the Q-mode, we selected a stretch of 1,000 continuous rotations between pulse numbers 150 and 1150 from the second observation on 2023-04-24, which we show in Fig. 11. This rotation range is ideal, as it is unusually long and almost free of RFI. We present the resulting LRFS in Fig. 12. The panels show the normalised pulse profile, the LRFS with the median off-pulse spectrum subtracted, the summed Fourier power spectral density (PSD) along the phase bin axis, and the phase-resolved Fourier-domain modulation index  $m$  computed from the LRFS. We trialed several FFT block sizes and window functions. A Hann window and FFT block length of 2000 rotations, i.e.  $2\times$  oversampling the data by zero padding, provides the most suitable frequency resolution. Three significant feature clumps are visible in the MP phase region. The left-most feature in Fig. 12 (feature 1) contains the maximum fluctuation power per bin and corresponds to a fluctuation period  $P_3 = (66.7 \pm 2) P_1$ . It aligns perfectly with the leading bump or shoulder in the MP profile. The feature is slightly extended in both pulse phase (15 phase bins) and towards lower fluctua-

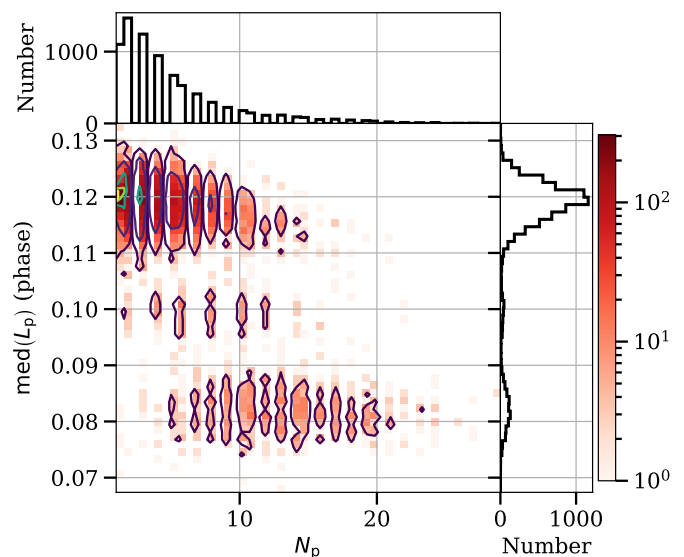
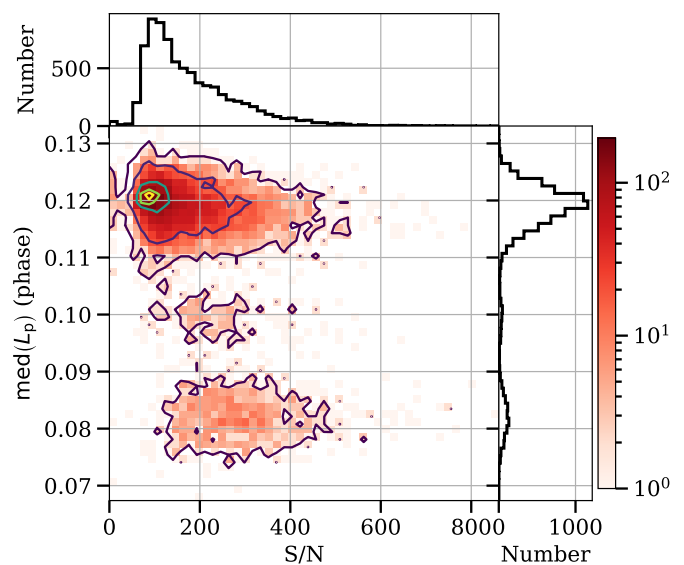
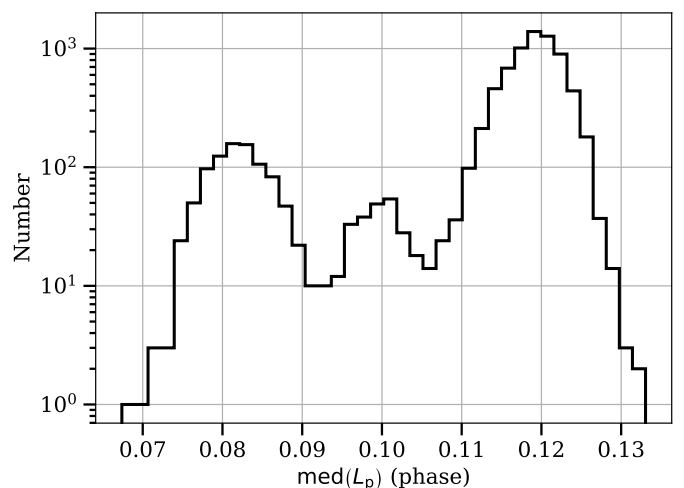


**Fig. 9.** Visual analysis of the number of emission modes present in the data. Top: 1D histogram of the median location of the peaked profile components shown in log scale. Middle and bottom: Two profile features plotted against each other in 2D (log scale) and 1D histograms (linear scale) on the sides. We show contours at 1, 10, 50, 75, and 90 per cent of the maximum bin count. The histograms indicate the presence of at least three stable emission modes in the pulsar and independently confirm our conclusions from the Markov model analysis.



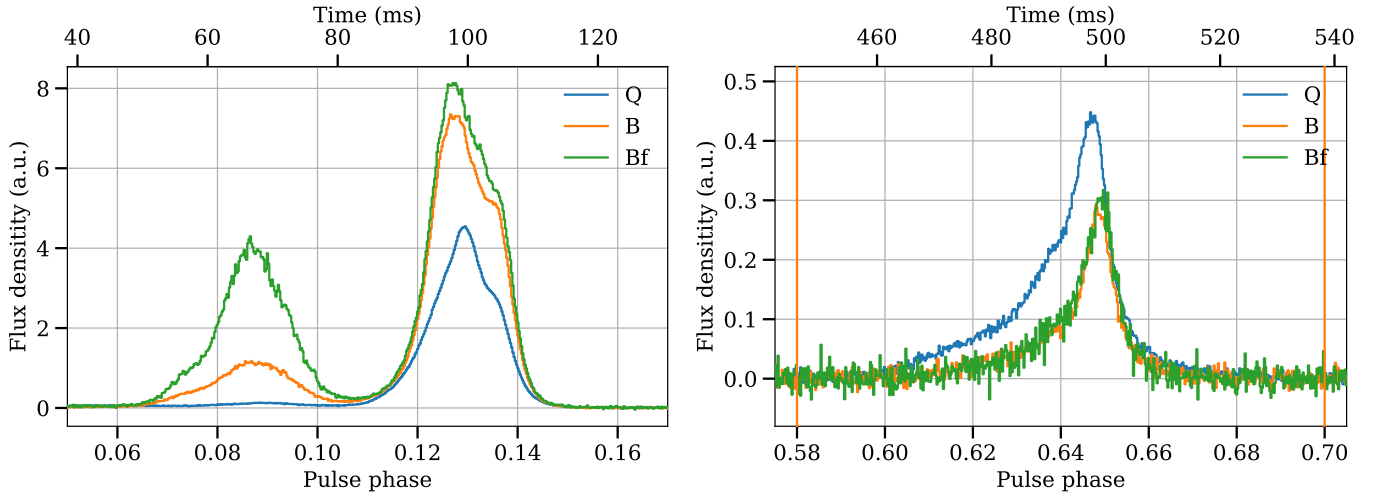


**Fig. 10.** Comparison of the mode-separated pulse profiles. The panels show zooms onto the combined PC and MP phase range (left) and the IP phase window (right). The quiescent Q-mode (blue), the bright B-mode (orange), and the bright flaring Bf-mode (green) are plotted on the same absolute scale.

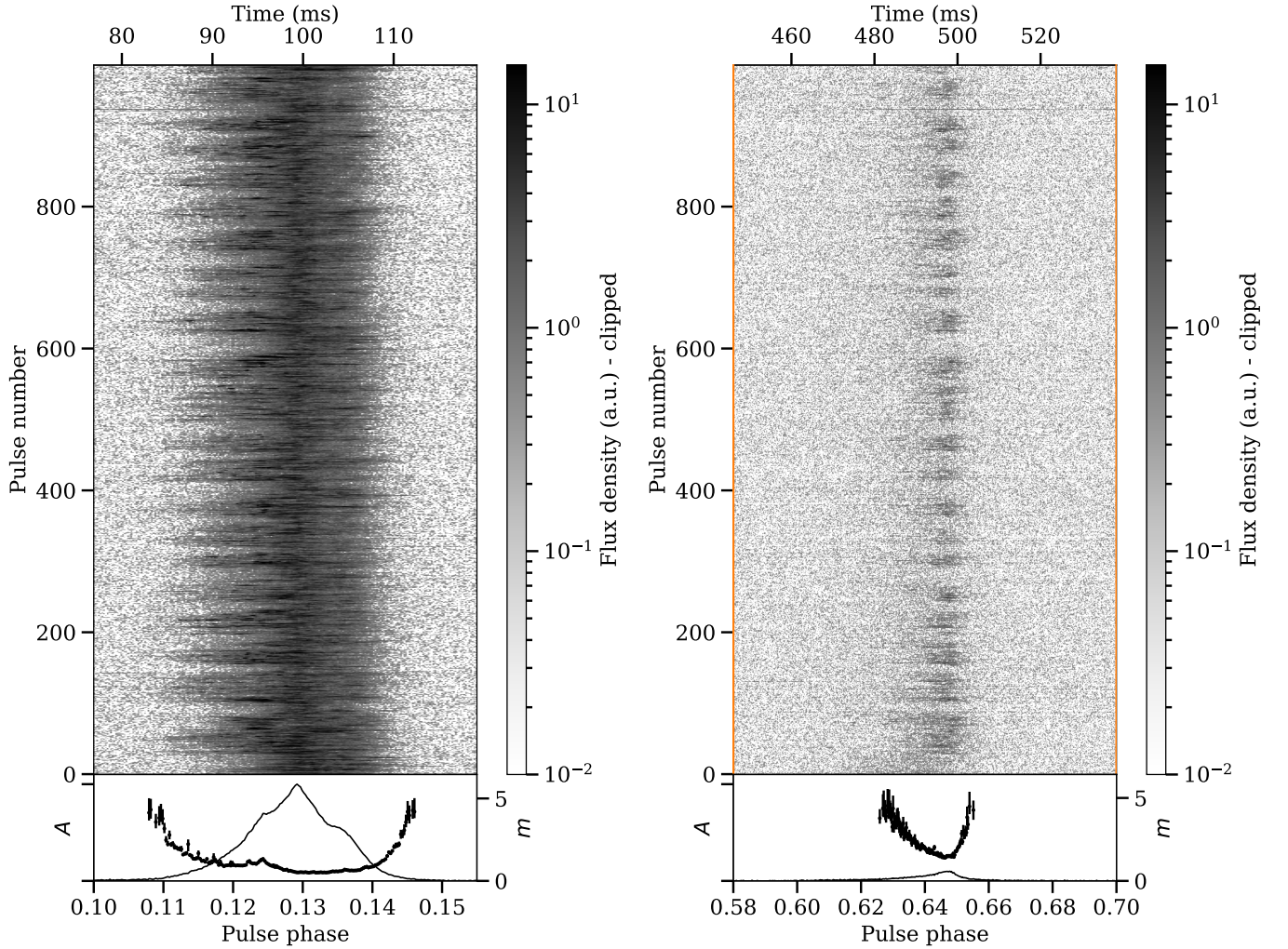


**Fig. 11.** Zoomed in and dynamic range compressed profile stack of 1,000 continuous rotations (pulse numbers 150 to 1150) of Q-mode emission taken from the second observation on 2023-04-24, as shown in Fig. 3 right panel. The bottom panels show the same parameters as in Fig. 3. We display the MP (left) and IP phase range (right) separately. A longitude-stationary amplitude modulation in the leading profile sub-component of the MP is clearly visible. The IP's intensity is modulated with the same period and synchronously with the MP's leading profile component.

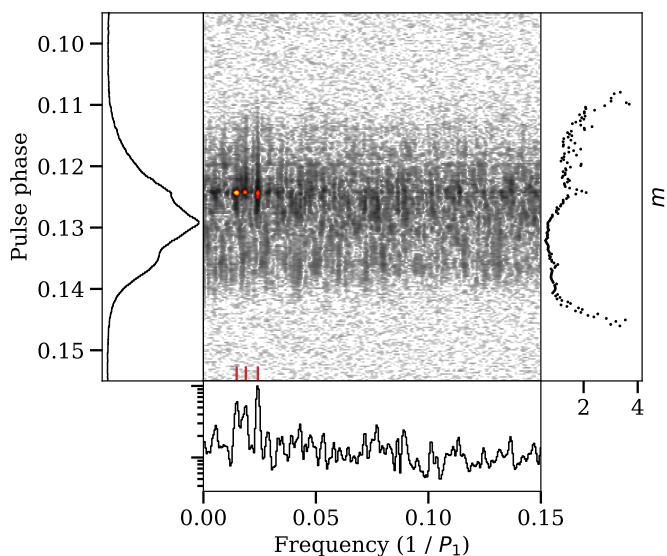


**Fig. 12.** LRFS of the pulse stack shown in Fig. 11. The FFT block size was set to 2000 rotations ( $2\times$  oversampling). The red-orange contours are drawn at 0.5, 0.6, 0.7, 0.8, 0.9, and 0.95 of the maximum fluctuation power spectral density and we zoomed into the area around the maximum. Three significant features are visible that align with the leading hump in the MP’s profile and the local peak in modulation index  $m$ . We marked their centroid frequencies with red vertical lines.

tion frequencies (7 FFT bins). The middle feature (feature 2) at  $P_3 = (52.6 \pm 1)P_1$  is narrow in fluctuation frequency (4 FFT bins) and fairly extended in pulse phase (55 bins). It seems to merge with feature 1 at lower frequencies. The right-most feature (feature 3) at  $P_3 = (41.7 \pm 0.9)P_1$  contains the maximum integrated power. It is reasonably narrow and well-defined in fluctuation frequency (4 bins), but extends significantly in pulse phase ( $\sim 73$  bins). Significant fluctuation power is visible between the pulse phases 0.11 and 0.128, which correspond to the onset of the MP profile at the leading edge and its profile peak. Interestingly, this FFT bin also contains excess power around the peak of the IP profile. Outside those phase ranges, the power in this FFT bin is consistent with the off-pulse noise. In fact, all three modulation features are replicated at lower intensity in the IP’s profile peak. The maximum power bins of all three features align in phase with each other, the leading hump in the MP’s profile, and the local maximum in modulation index. Hence, they seem to be genuinely different fluctuation periods in the same profile sub-component. There is no significant fluctuation power in the off-pulse phase range, which indicates that instrumental effects are well suppressed. We quote all the fluctuation periods above at the centres of the maximum amplitude FFT bins and state uncertainties corresponding to one FFT bin width.

Our 2dFS analysis nicely recovered the  $P_3 = 41.7 P_1$  feature and its harmonics in the MP. The feature is narrow in  $P_3/P_1$  space (2 bins) and slightly extended in  $P_2$  space (5 bins). Its fluctuation power peaks in the first non-DC bin in the  $P_2$  domain, i.e. its maximum is offset by only one bin from the vertical axis. In other words, its  $P_2$  is consistent with zero. Therefore, the feature is most likely caused by a longitude-stationary amplitude modulation and not a sub-pulse drifting (phase) effect. The amplitude modulation or oscillation of pulse intensity in the MP’s leading profile sub-component is clearly visible in the zoomed in pulse stack shown in Fig. 11 left panel. We separately performed a 2dFS of the IP and the  $P_3 = 41.7 P_1$  modulation is also present there. Both the MP’s leading component and the IP’s overall in-

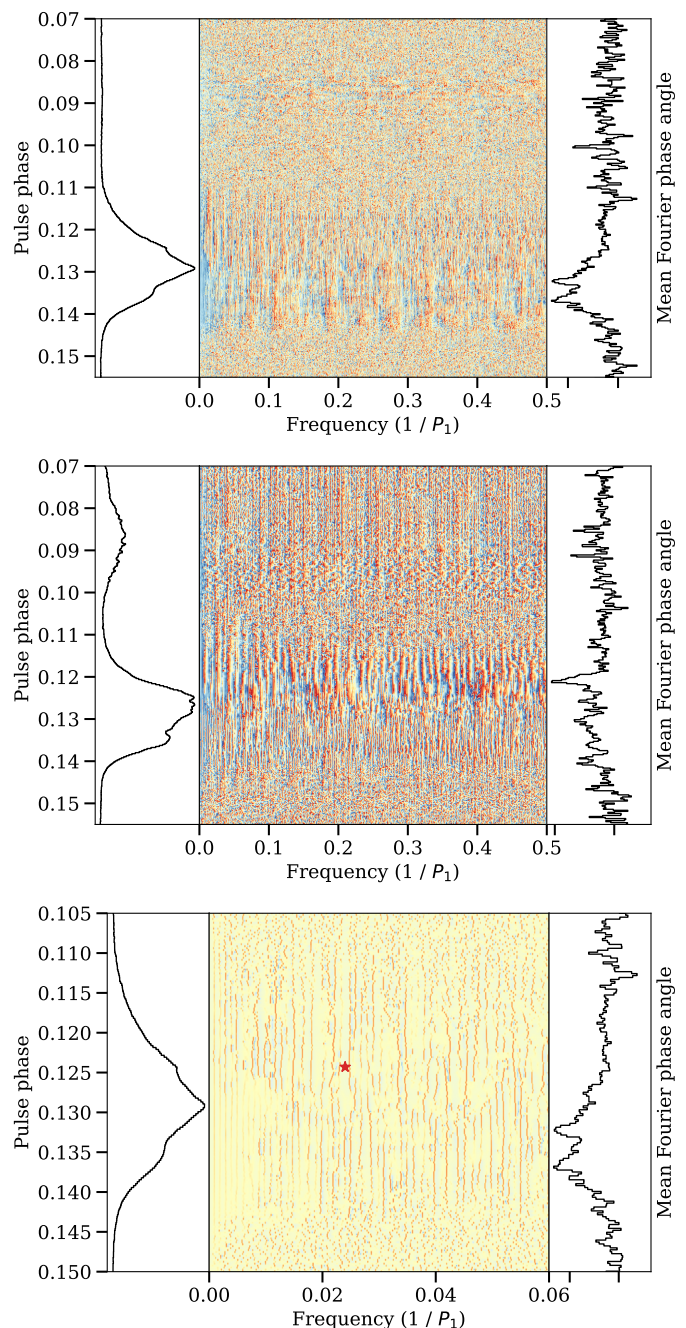


**Fig. 13.** Longitude-resolved phase angle spectra (LRPS) of the Q-mode (top) and B/Bf-mode emission (middle). The FFT block size was set to 8,000 and 1,680 rotations, which corresponds to eight and four times oversampling. Bottom: phase angle gradient along the frequency axis of the Q-mode LRPS from the top panel. We zoomed into the area near the  $P_3 = 41.7 P_1$  modulation feature shown with a star marker.

tensity are modulated with the same period and synchronously with each other, i.e. positively correlated in flux density or fluence (Fig. 11). This phase-locked relationship between the MP and IP within the Q-mode is a new discovery, as far as we know.

We repeated our analysis for the pulsar’s B- and Bf-mode emission. We selected the pulse number range from 2990 to 3410 of the second observation on 2024-04-24, as shown in Fig. 3 right panel. This is the longest continuous B/Bf-mode emission stretch in our data. We averaged up to eight oversampled LRFS periodograms using Welch’s algorithm (Welch 1967) with



a Hann window to reduce and smooth the noise floor. There are several peaks visible in the LRFS below  $0.11 P_1^{-1}$  whose maximum power bins align with a subtle bump (phase range 0.121 to 0.124) at the leading edge of the MP's profile just before the first local peak. However, they are only marginally above the integrated noise floor ( $\leq 3\sigma$ ). Aside from those, there is no clear periodicity visible in the LRFS. The 2dFS confirmed the absence of any obvious modulation.

To investigate the single-pulse modulation further we computed what we call a longitude-resolved phase angle spectrum (LRPS), which is analogue to the LRFS. It visualises the phase angle of the complex Fourier coefficients for all fluctuation frequencies and phase bins. The mean complex off-pulse spectrum was subtracted before computing the angles. We show the resulting LRPS in Fig. 13 for the Q-mode and B/Bf-mode pulse stacks described above. We oversampled the data by zero-padding the FFT by a factor of eight and four times, respectively. The panels in Fig. 13 show the normalised pulse profile, the LRPS, and the mean Fourier phase angle computed along the fluctuation frequency axis. We mapped negative phase angles to blue shades, zero to yellow, and positive angles to red shades. The red and orange horizontal lines denote the on-pulse phase ranges as in the other figures. The LRPS shows the phase relation between different Fourier components, i.e. how they align in phase with respect to each other. The MP LRPS are strikingly different between the modes. The Q-mode (Fig. 13 top panel) shows relatively large patches of similar phase angle that are adjacent in bin and frequency space. The  $P_3 = 41.7 P_1$  modulation feature at  $0.024 P_1^{-1}$  sits right in the middle of one of the “ridge lines” at approximately zero phase angle in a low negative gradient ( $-25$  deg) area (star marker in Fig. 13 bottom panel). There is a large patch of mostly negative phase angle at fluctuation frequencies below  $0.012 P_1^{-1}$  that extends from the MP's profile leading hump to its trailing flank. A similar patch is also visible in the IP. This low-frequency red noise is most likely due to scintillation or a pulsar intrinsic coherent noise process. It is interesting how that area appears to be smoothed out to an almost constant angle. The mean phase angle is noticeably negative across the MP, particularly starting from the leading hump until the trailing end. The maximum negative excursions of  $-13$  deg happen symmetrically around the trailing saddle point in the profile. There is also a hint of low-level PC emission visible at small fluctuation frequencies  $\leq 0.1 P_1$ . In contrast, the B/Bf-mode LRPS (Fig. 13 middle panel) shows rapid phase angle variation with fluctuation frequency. The MP's trailing edge looks unstructured and almost randomised, while the leading edge exhibits narrow regularly occurring patches of rapid negative phase angle sweep. There are no clear structures visible in the PC apart from the negative angle smoothing at low fluctuation frequencies. The angle changes rapidly with frequency. The IP LRPS looks qualitatively similar between the modes. The difference is primarily in patch intensity and that the Q-mode looks smoother. Overall, the phases change more smoothly in the Q-mode, whereas the B/Bf-mode shows more rapid phase angle variation and appears more chaotic. This agrees with our intuition gained from looking at the pulse stacks and single-pulse profiles.

### 3.2.5. Asynchronous mode-switching of the MP and IP

When looking at the single-pulse stack in a logarithmic greyscale (Figs. 3–4), we noticed that the IP emission is wider and somewhat brighter when the pulsar is in the Q-mode in the MP region. When the B/Bf-mode mode is active in the MP, the IP is significantly narrower and fainter. We investigated this by ex-

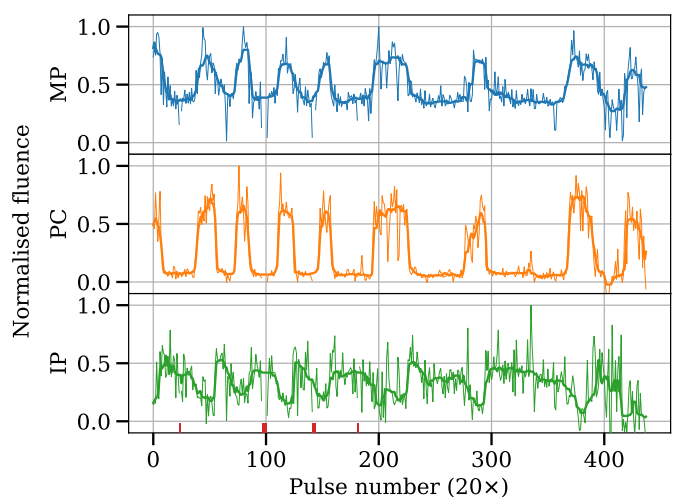


**Fig. 14.** Correlation analysis between the emission in the MP, PC, and IP phase regions. We show time series of the measured on-pulse fluences normalised by their individual maxima, where we averaged every 20 pulses for clarity. The solid lines depict running median smoothings of the data using 10-sample wide sliding windows. The red markers at the bottom highlight integrations that were excised. The MP and PC components switch fluence synchronously to each other, while the IP switches asynchronously to both the PC and MP. The latter strongly suggests a feedback mechanism between the polar caps on opposite sides of the star.

tracting time series of fluence and boxcar equivalent pulse width separately in the PC (0.01 – 0.107), MP (0.107 – 0.2) and IP (0.58 – 0.7) phase ranges. These are shown in Fig. 14, where we averaged every 20 pulses to increase the S/N. To reduce the noise further, we computed median smoothings of the time series with 10-sample (200 rotation) wide sliding windows. Those are shown as solid lines. The MP shows an almost constant fluence in the Q-mode, which approximately doubles when it enters the B/Bf-mode. This is not just because of the appearance of the PC component; the MP indeed gets brighter in both peak and component averaged flux density. At the same time, the PC fluence increases by a factor of  $\sim 10$  from being almost consistent with the baseline noise. The dynamic range is significantly higher than in the MP. The IP fluence timeline is much noisier because of its small absolute value, but increases by a factor of  $\sim 3$  after the pulsar switches to the Q-mode. Fig. 14 also shows the almost perfect correlation between the moding in the different profile components. The PC and MP switch fluence synchronously to each other and asynchronously to the IP. The same behaviour can be seen in the boxcar equivalent pulse width. This means that there exists a feedback between the emission emanating from opposite poles of the star. The switching of the magnetosphere between the stable emission configurations on the one side of the star must interact with that at the opposite magnetic pole. Hence, there must exist a feedback mechanism and information transfer between both polar caps, as was pointed out already early on (Fowler & Wright 1982; Dyks et al. 2005).

### 3.3. Single-pulse profile morphology, dynamic spectra, and microstructure

With the aim of characterising PSR B1822–09's single-pulse profile morphology and emission characteristics, we visually inspected the 8,743 single-pulses in the observation taken on 2023-04-24. We found several peculiar single-pulse phenomena in the



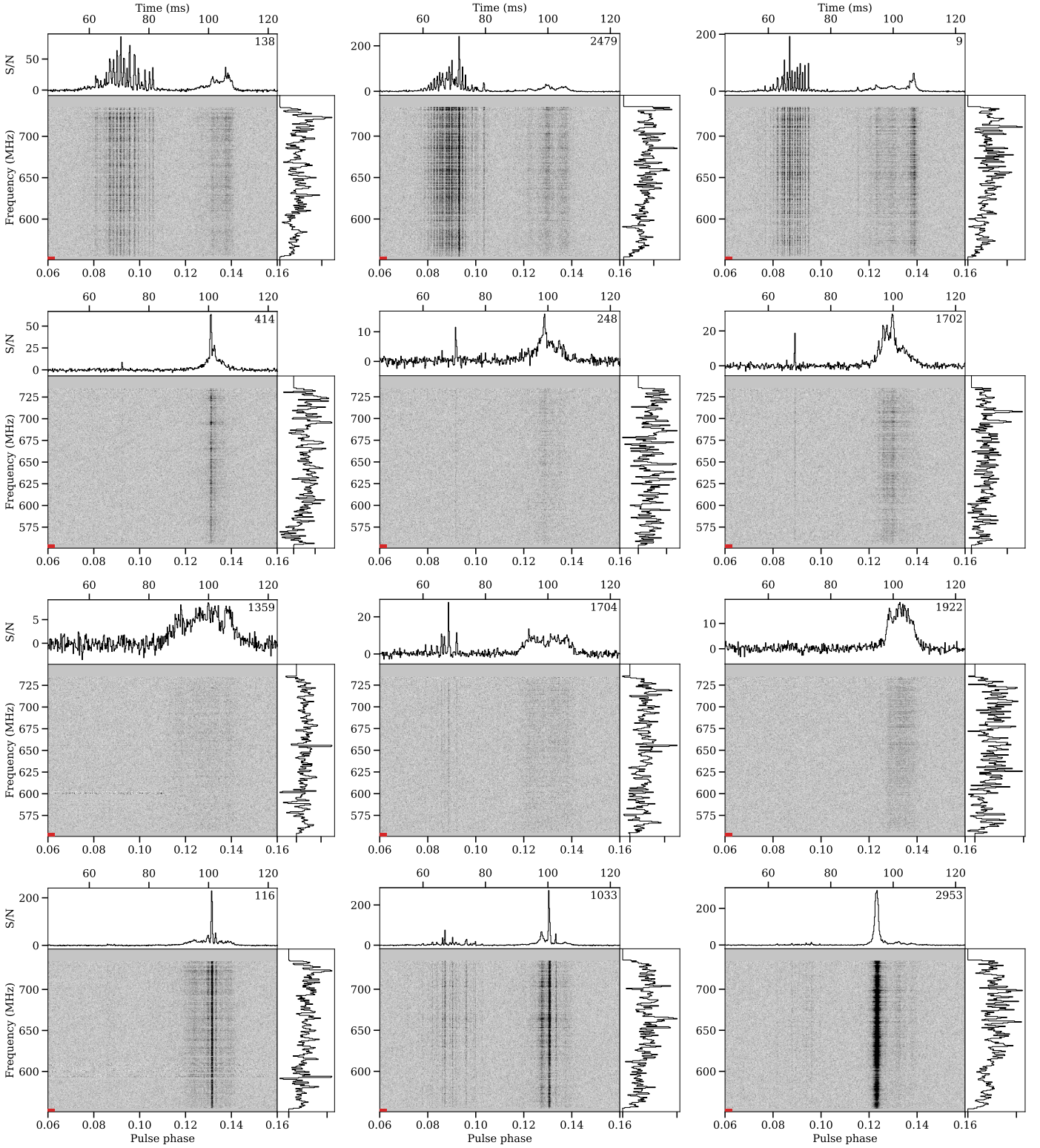


**Fig. 15.** Three representative examples each of single-pulses with extensive quasi-periodic microstructure (top row), low-level PC activity within long stretches of Q-mode emission (second row), low-intensity square-like pulses (third row), and extremely bright pulse components (bottom row), as observed in the PC and MP phase range. We display the pulse numbers in the top right corner of the profile panels. The dedispersed dynamic spectra are saturated at the same intensity in each panel.

data that we describe below. In Fig. 15 we show three representative example single-pulses of each phenomenon.

### 3.3.1. Quasi-periodic microstructure in the PC component

Firstly, the most striking feature is the quasi-periodic microstructure seen primarily in the PC pulse profile component when the pulsar is in the Bf-mode (Fig. 15 top row). We show additional

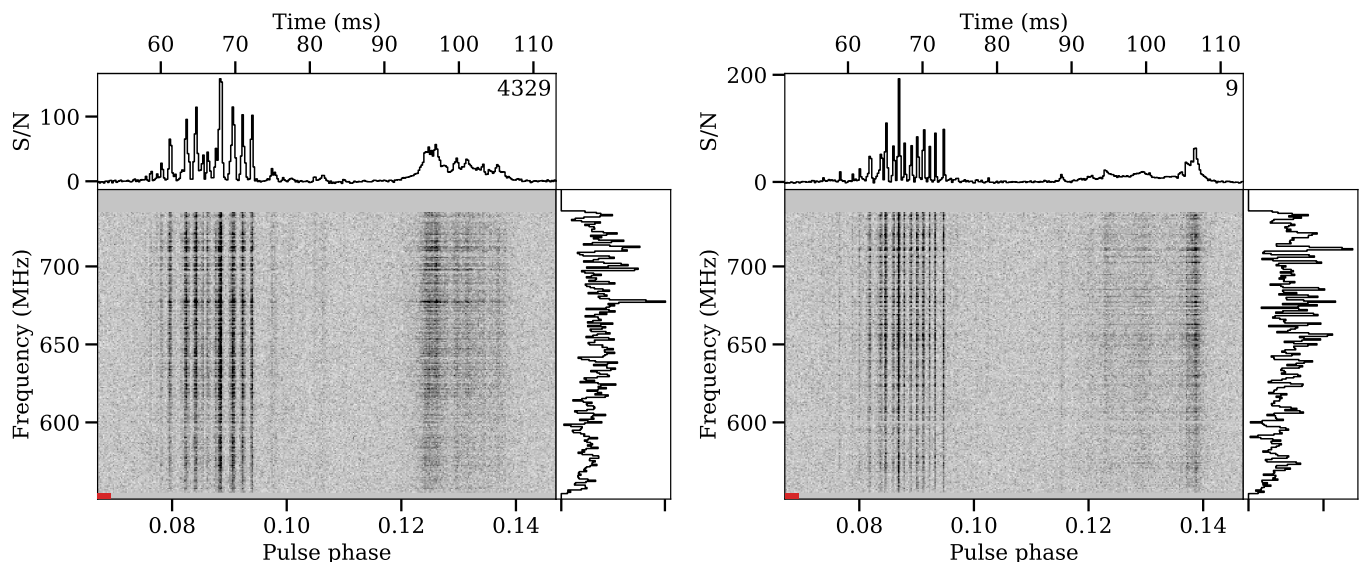


**Fig. 16.** Dedispersed single-pulse dynamic spectra zoomed into the PC and MP profile components. Quasi-periodic microstructure is clearly visible in the PC pulse envelope in those example pulses.

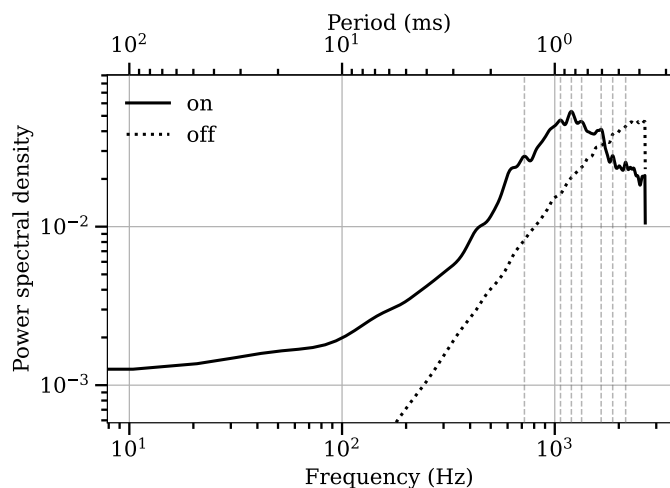


**Fig. 17.** Fourier power spectral density averaged over 59 single-pulses that exhibit extensive quasi-periodic microstructure in the PC profile component. The black solid line shows the sample mean and the grey shaded area its standard error for the combined PC and MP on-pulse phase range. The black dotted line is the same for the off-pulse region. The grey dashed lines mark significant features. The dominant feature occurs near 1200 Hz, or 0.83 ms.

example single-pulses that exhibit extensive PC microstructure in Fig. 16. As can be seen, the PC consists of extremely narrow (1 – 2 bins wide) microshot-like emission that can be very bright with up to  $S/N \geq 200$  per phase bin. The microshots often occur quasi-periodically within the PC phase window, as is evident from Figs. 15 – 16. We analysed their quasi-periodicity in the frequency domain by computing the Fourier power spectral density (PSD) using Welch’s algorithm with a Hann window on the first difference of the pulse profile time series, i.e.  $\delta_i = A_{i+1} - A_i, \forall i \in [0, N_{\text{on}} - 1]$ , where  $A_i$  is the Stokes I profile amplitude at the phase bin  $i$ , and  $N_{\text{on}}$  is the number of on-pulse phase bins. Taking the profile difference is beneficial, as it suppresses any low-frequency red noise. The differencing operation effectively acts as a high-pass filter. Additionally, we performed

an autocorrelation function analysis for comparison and computed time-resolved spectrograms using the short-time Fourier transform and wavelet scalograms to understand the temporal evolution in frequency across the pulse profile. We then stacked and averaged the Fourier PSDs of 59 single-pulses that show strong PC microstructure. Fig. 17 shows the resulting mean PSD and its standard error for the combined PC and MP on-pulse phase region (on) and the off-pulse phase range (off) for comparison. We highlighted several PSD features with vertical grey dashed lines. These occur near 720, 1064, 1197, 1337, 1652, 1872, and 2154 Hz, which corresponds to periods of 1.39, 0.94, 0.84, 0.75, 0.61, 0.53, and 0.46 ms. The quasi-periodicity near 1197 Hz (0.84 ms) clearly dominates the PSD. This means that microshots typically occur roughly every 0.8 ms within the PC envelope, which agrees well with our visual profile inspection. The mean off-pulse PSD is smooth and featureless from 8 Hz up to the Nyquist frequency, which indicates that instrumental effects are well suppressed. Thus, our Fourier analysis unambiguously confirmed the quasi-periodic emission.

We were then interested in the temporal extent and separation of the microshots. We investigated this by automatically identifying the peaked profile components above 10 S/N in the time domain and measuring their number, S/N, half-prominence widths, and separations for the same set of single-pulses with extensive PC microstructure as before and as visualised in Fig. 5. The number of microshots in the PC and MP phase window ranges between 14 and 34 with a peak in histogram counts between 19 and 21. The full-width half-prominence histogram has a broad top with almost equal counts between 0.22 and 0.41 ms, which corresponds to 1.2 and 2.2 phase bins, and falls off rapidly afterwards. The mode of the distribution of pulse separations (centre-to-centre) between consecutive profile peaks lies between 0.73 and 1.08 ms, or 3.9 and 5.8 phase bins, and falls off quickly. However, there is a minor bump near 2.9 ms (15.5 bins), which is probably due to the microstructure within the MP. Additionally, there is a very slight and broad accumulation of counts between 16 and 27 ms, which are the separations between the last peak of the PC and the first of the MP, i.e. the PC – MP profile component separation. The S/N histogram shows a maximum S/N per phase bin of 240 with an almost exponential in-



crease towards lower values and a mode near 12. Interestingly, the phase resolution of our single-pulse folded data ( $187.74 \mu\text{s}$ ) seems to resolve the majority of the microshots. The mode of the width distribution is appreciably offset from the resolution limit and the distribution approximately halves before reaching the threshold. However, the broad flat top of the distribution might point towards a pile-up. The native time resolution of our data ( $81.92 \mu\text{s}$ ) will allow a more detailed investigation in the future. Our analyses in the frequency and time domain agree nicely.

In a subsequent step we examined where in the single-pulse stacks the pulses with strong PC microstructure happened and whether they were temporally related with any of the other single-pulse phenomena described below. They appear only during the B/Bf-mode and typically occur in small clusters or bursts where two to four pulses show extreme microstructure in almost consecutive pulses. In fact, there are several occasions where we see strong PC microstructure in truly consecutive pulses. Some microshots remain phase-aligned in those consecutive pulses, i.e. static in phase between rotations, while most vary slightly in phase location, amplitude, and width to a lesser extent. Those small clusters are usually separated by 20 – 30 rotations and this cluster pattern repeats roughly uniformly during the B/Bf-mode activity window. There is no clear discernible pattern with respect to the MP’s brightness, pulse width, or microstructure. The PC’s microstructure behaviour seems mostly independent from the MP emission. The clusters of extensive PC microstructure and bright pulses in the MP (flaring) alternate, with the occasional alignment close in rotation space, but without any obvious pattern. Similarly, there is a lack of correlation with the other single-pulse phenomena.

In summary, we find that the narrow emission components are indeed quasi-periodic microshots with typical full-widths at half maximum between 0.2 and 0.4 ms and usual separations between 0.7 and 1 ms. The most prevalent quasi-periodicity occurs with a frequency near 1.2 kHz or a period of 0.83 ms. There are typically 20 microshots in the combined PC and MP phase range.

### 3.3.2. Mode mixing

Secondly, the pulsar occasionally clearly shows low-level PC activity within long stretches of what appears as otherwise pure Q-mode emission. We show examples of this in Fig. 15 second row. In those pulses, only one or two very narrow (2 – 4 phase bins) peaked emission components are visible above the baseline noise in the PC phase range 0.07 – 0.1. Their peak S/N is low compared with the MP emission, ranging from 0.1 to 0.7 of the maximum MP S/N. The pulses occur within the PC phase envelope and are sufficiently distant from the MP. Hence, they genuinely come from the PC and are unlikely due to bridge emission between the two profile components. In a subsequent step, we highlighted the rotations with low-level PC activity as identified from the dynamic spectrum plots on the single-pulse stacks. Guided by the markers, the PC activity becomes faintly visible in the pulse stacks. For instance, we see low-level PC emission in the pulse number ranges 274 – 318, 1232 – 1267, 1744 – 1893, 2508 – 2598, 3181 – 3258, and 3701 – 3724 in the first pointing on 2023-04-24 (Fig. 3 left panel). In the second pointing (Fig. 3 right panel), we see low-level PC activity in the rotation ranges 77 – 272, 1521 – 1612, and 1700 – 1715. That is, the PC emission stays active at a significantly reduced level for about 50 – 100 rotations after a mode-switch from the B/Bf-mode to the Q-mode. At other occasions, the PC emission activates randomly during a long Q-mode stretch several hundred rotations after a mode-

switch. This appears to happen preferentially near the middle of a given Q-mode stretch. The reverse is true as well. There are many rotations within otherwise pure B/Bf-mode emission stretches where the PC profile component is entirely absent. Additionally, the pulse number range 3701 – 3724 in the first pointing shows another peculiar behaviour. The PC becomes active for several rotations in this region far away from the previous mode-switch. One might think that the pulsar briefly switches to the B/Bf-mode, but this is not the case. The MP lacks any noticeable change, the PC emission exhibits a lower intensity, smaller  $N_p$ , and is shifted to later pulse phases (0.1) compared with the typical B/Bf-mode PC contribution. The same is apparent from the feature timelines in Fig. 6. Hence, this pulse number range might show an entirely new and distinct emission mode of the pulsar.

The low-level activity of the PC after a switch to the Q-mode and spuriously within long otherwise pure Q-mode stretches indicates clearly that the pulsar exhibits mode mixing. This is surprising, as it goes against conventional pulsar knowledge (Hermesen et al. 2017). It seems that several modes can be simultaneously active in the pulsar, which also means that there is no binary classification (PC on vs. off) into disjoint modes possible. In other words, the currently observed emission state of the pulsar is likely a weighted sum of its (disjoint) emission modes, where the mixture weights determine the various contributions. For instance, during the Q-mode the contribution that drives the PC emission might have an almost negligible weight, whereas during the B/Bf-mode it might reach its maximum.

### 3.3.3. Low-intensity square-like pulses

Thirdly, we discovered strangely looking almost featureless pulses with very low S/N  $\leq 5 - 10$  per phase bin. A less sensitive telescope might register them as nulling. Some of them have almost square like appearance (Fig. 15 third row) with boxcar-equivalent widths between 0.01 and 0.03 phase (8 – 23 ms). The low-intensity pulses occur irrespective of mode, i.e. they appear during both long Q-mode and B/Bf-mode pulse stretches. They often occur clustered in time with two to four low-intensity pulses after each other. They are fairly common in our single-pulse selection and the overall pulse stack, with relative occurrences between 30 and 40 per cent. We speculate that these low-intensity square pulses are produced by the most stable emission components in the pulsar’s magnetosphere. They might resemble a stable baseline or plateau emission in the MP window. In principle, they might be evidence for a fourth emission mode of the pulsar, although our current Markov switching model implementation did not identify them as such.

### 3.3.4. Flaring emission in the MP component

Moreover, the MP shows rare extremely bright bursts of emission of S/N  $\geq 100 - 200$  per phase bin, always occurring in a specific pulse phase range near the centre of the MP window, during which the overall emission is dominated by that single peak (Fig. 15 bottom row). There seems to be some interplay between the occurrence of the extremely bright pulses and the mode-switching in the sense that the bright pulses typically happen shortly after a mode transition to the B/Bf-mode.

To investigate the bright pulses further, we measured the empirical pulse-energy (PE) distributions in separate phase ranges for each of the profile components (MP, PC, and IP) and the off-pulse baseline noise. We show the mode-averaged PE distri-



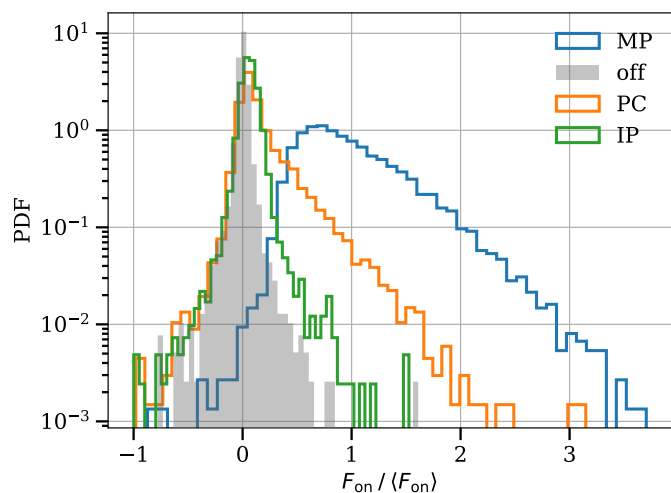


**Fig. 18.** Mode-averaged pulse-energy distributions for each profile component (MP, PC, and IP) and the off-pulse baseline noise. The MP and PC distributions exhibit log-normal high-fluence tails and lack any obvious power-law behaviour.

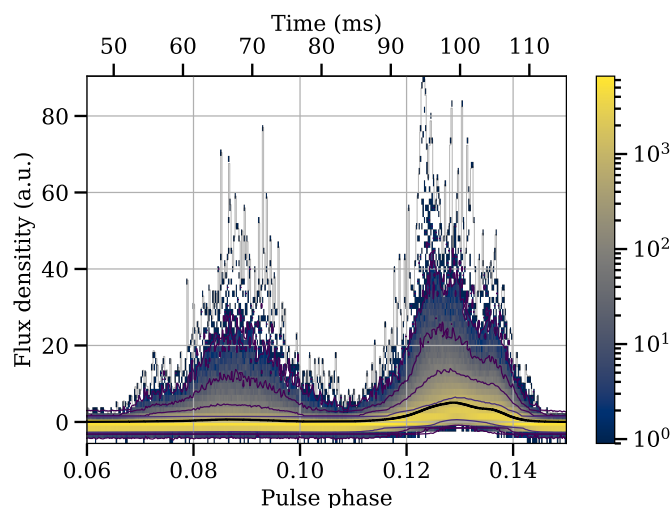


**Fig. 19.** Phase-resolved single-pulse amplitude distribution of the PC and MP phase range. We show the 2D amplitude-phase distribution, i.e. the number of pulses per flux density and phase bin, displayed on a logarithmic colour scale. The black solid line is the average pulse profile, the grey solid line the maximum amplitude, and the coloured solid lines are logarithmically spaced contours of the 2D distribution.

distributions referenced to a constant global mean on-pulse fluence  $\langle F_{\text{on}} \rangle$  in Fig. 18. The MP PE distribution is almost perfectly described by a log-normal distribution. The PC distribution is a mixture between a Gaussian at low and a log-normal distribution at higher fluences, which likely represent the Q- and B/Bf-mode contributions. The IP PE distribution differs only slightly from a normal distribution. There is a slight peak at  $0.8 \langle F_{\text{on}} \rangle$  and the distribution is positively shifted, appreciably above the off-pulse noise. The off-pulse distribution is well-described by a Gaussian, as expected from being primarily due to radiometer noise. The measured PE distributions lack any obvious power-law shape in a double logarithmic plot, besides a suggestive linear slope in the low-fluence PC distribution below  $0.6 \langle F_{\text{on}} \rangle$ . Additionally, the high-fluence distribution tails show clear curvature in the same double logarithmic plot. Hence, the bright pulses are unlikely giant or micro-giant pulses. There is no evidence for this in our

data set. The brightest pulses reach about 3.7 (MP), 3.1 (PC), and 1.5 (IP) times the MP mean on-pulse fluence  $\langle F_{\text{on}} \rangle$  averaged over their respective phase ranges.

To understand where in the on-pulse envelope the bright pulses originate, we generated phase-resolved single-pulse flux density amplitude distribution plots. Fig. 19 shows the 2D amplitude-phase distribution in a logarithmic colour scale and contours. As is apparent, the brightest MP pulses occur predominantly at earlier phases near  $0.123 - 0.125$  at the leading edge of the MP. Additionally, there is a slightly lower peak near  $0.129$  phase, which is close the MP's profile maximum. The brightest pulses exceed the average by a factor of 30 in intensity per phase bin. This agrees well with our visual inspection and the example plots shown in Fig. 15. The bright pulses seem to be created by flaring or bursting events near the leading edge of the MP, where the MP profile component widens slightly towards earlier phases. Those flaring events can even be seen in the pulse stacks in Figs. 3 – 4.

The situation is somewhat different for the PC, where the emission of narrow bright micro-pulses occurs relatively uniformly across the PC phase window. There is a marginal clustering near  $0.087 - 0.088$  phase, which is near the PC's local profile maximum. The brightest PC pulses exceed its mode-averaged mean emission by a factor of 150.

### 3.3.5. Pulse intensity fading after mode-switches

Additionally, we noticed that the intensity of the pulses slowly increases or fades in after a mode-switch to the B/Bf-mode and fades out after the switch back to the B-mode. Besides the single-pulse profiles and dynamic spectra, one can also see this behaviour in the  $F_{\text{on}}$  and S/N feature timelines in Fig. 6, where the grey running mean lines help guide the eye. It seems that the pulsar needs some time to reach its maximum average radio intensity in that mode. The low-level PC activity in the Q-mode that we discovered and described earlier likely contributes to the fading out of the pulsar's intensity after the switch.

## 4. Discussion

### 4.1. Mode-switching behaviour

PSR B1822–09 has been known to exhibit two distinct emission modes (Q and B-mode) for a long time (Fowler et al. 1981) and has been an example for a classical mode-switching pulsar. Here we presented strong evidence for the existence of at least a third distinct emission mode in the pulsar, which we called the bright flaring Bf-mode. It is characterised by a higher pulse-averaged flux density, more extreme sub-millisecond microstructure emission in the PC, and a significantly higher contribution of the PC to the pulsar's total flux density output. In particular, the fluence ratio between PC and MP is more similar than in the other modes, at around 1:2 (Fig. 10). Because of those properties, we consider it to be a flaring emission mode. The separation from the regular B-mode is clear and most obvious in the  $N_p$  domain (Fig. 7). In many regards, it is a more extreme version of the ordinary B-mode. Our Markov switching model identified it confidently as a distinct emission mode. Apart from the obvious differences in microstructure at the single-pulse level, the ratio of the component-integrated PC to MP fluence differentiates the three modes (Fig. 10).

Interestingly, this is analogue to the amplitude ratio shape parameter  $A_{\text{pc}}/A_{\text{mp}}$ , where  $A_{\text{pc}}$  is the amplitude of the PC and  $A_{\text{mp}}$  that of the MP, that correlates with the pulsar's spin-down rate  $\dot{\nu}$

on timescales of several years (Lyne et al. 2010). It might simply be that the pulsar on average switches more often into the flaring Bf-mode during its times of high- $\dot{\nu}$  (Fig. 5 of Lyne et al. 2010). Or in reverse, a more frequent switching to the Bf-mode on average results in a higher energy output, which in turn causes the star to spin down faster, i.e. a higher dipole magnetic braking and higher  $\dot{\nu}$ . In our Markov switching model for the pulsar's moding, this behaviour can naturally be explained by a slight increase in the transition probability  $p_{21}$  from the B-mode to the Bf-mode or potentially also directly from the Q-mode (Fig. 8). This would result on average in a higher presence of the Bf-mode. However, it is not obvious what physical mechanism could alter the pulsar's intrinsic state transition probabilities. One could invoke an external perturbation of the pulsar's magnetosphere by an asteroid or other dense material from an accretion disk for example. In this picture, the transition probability might decay over several years back to its original value as the system slowly returns to its original (unperturbed) state. This hypothesis is consistent with the observed return of the pulsar to its original  $\dot{\nu}$  value.

In terms of pulsar energetics, an increase in radio energy output alone is not enough. The excursions in  $\dot{\nu}$  have roughly  $\Delta\dot{\nu} \approx 3\%$  (Fig. 5 of Lyne et al. 2010), and thus the spin-down luminosity must increase by the same amount,  $\Delta\dot{E} \approx 3\%$ . A pulsar with  $\dot{E} \approx 4.5 \times 10^{33}$  erg/s might have a radio efficiency  $\xi_r = 10^{-5} - 10^{-3}$  (Szary et al. 2014). We know from observations that the X-ray emission does not participate significantly in the mode-switching in this pulsar (Hermsen et al. 2017). A  $\gamma$ -ray pulsar with comparable  $\dot{E}$  to PSR B1822-09 has a  $\gamma$ -ray efficiency around  $\xi_\gamma = 5\%$  with a large uncertainty (Smith et al. 2023). So in principle, an increase in  $\gamma$ -ray energy output could account for the 3%  $\Delta\dot{E}$ . However, B1822-09 is only faintly detected in MeV  $\gamma$ -rays, which suggests that its  $\xi_\gamma$  is significantly lower than 5%, or that we only see a small part of its  $\gamma$ -ray emission. To resolve the problem, one could invoke an unseen wind of energetic particles that carries away the spin-down luminosity difference, and which might switch in tandem with the radio emission.

Additionally, we found evidence for mode mixing, i.e. the presence of clear PC activity within long otherwise pure Q-mode stretches (Fig. 15). This challenges the traditional assumption that the pulsar emission modes are fully disjoint and presents complications for modelling the mode-switching process, including our own Markov switching model.

#### 4.2. Fluctuation properties

Our results for the  $P_3 = (41.7 \pm 0.9) P_1$  Q-mode modulation feature are in good agreement with the literature. In particular, Yan et al. (2019) reported a periodicity of  $P_3 = (42.6 \pm 0.2) P_1$  at 1.4 GHz. Backus et al. (2010) found  $P_3 = (43.75 \pm 1.0) P_1$  at 325 MHz. Earlier work suggested a  $P_3 \approx 40 P_1$  at 1.4 GHz (Gil et al. 1994) and 1.6 GHz (Fowler et al. 1981). Those values are entirely consistent within the uncertainties. However, there is a slight  $\sim 3 \sigma$  tension with the measurement of  $P_3 = (46.55 \pm 0.88) P_1$  at 325 MHz reported by Latham et al. (2012). We believe that most of the variation can be attributed to how the maximum Fourier power bin was determined in the LRFS and the presence of spectral leakage if not accounted for by windowing the FFT. Overall, the  $P_3$  Q-mode modulation is stable in time over more than 40 years and a factor of five in observed radio frequency.

It is interesting that the longer period fluctuation features we found at 52.6 and 66.7  $P_1$  have not been reported in the literature. They are of lower Fourier S/N, but clearly above the noise floor

and distinct from the 41.7  $P_1$  feature in the LRFS (Fig. 12). We suspect that our long Q-mode data stretch (1,000 rotations), absence of RFI, and excellent data quality enabled their detection.

Our analysis indicates that the Q-mode fluctuation is primarily or solely due to longitude-stationary amplitude modulation. There is no evidence of sub-pulse drifting. This agrees with previous work at 1.4 GHz (Gil et al. 1994; Yan et al. 2019), but is in tension with the analyses performed at 325 MHz that suggested a phase or amplitude-phase modulation (Backus et al. 2010; Latham et al. 2012). This might suggest a transition in Q-mode fluctuation character from pure phase or mixed amplitude-phase modulation at low frequencies to primarily amplitude modulation at 650 MHz and above. Alternatively, rapid diffractive interstellar scintillation of the pulsar's radio signal could potentially have induced extrinsic phase modulation in earlier work if the pulsar's radio spectral index varied considerably across the MP envelope and the instrumental band was small compared with the scintillation bandwidth, i.e. due to insufficient spectral averaging of older narrow-band data.

We found no evidence for modulation in any of the profile components in our B- and Bf-mode data. In particular, there was no obvious modulation at the previously reported periods of  $P_3 = 11 P_1$  (Fowler et al. 1981; Gil et al. 1994) or  $P_3 = 70 P_1$  (Latham et al. 2012).

#### 4.3. Is the periodic Q-mode amplitude modulation caused by mode-switching?

Yan et al. (2019) discussed the Q-mode modulation in the context of longitude-stationary amplitude modulation and periodic nulling. They concluded that it is the former that happens. Indeed, we did not find any evidence for nulling in our data set. The pulsar emitted continuously during each rotation that was unaffected by RFI, as we show in Figs. 3–4, 11, and 14. Hence, it is not nulling that is responsible for the modulation. Another possibility is that the modulation is caused by subtle mode-switches. Our hidden Markov model considered all low  $N_p$  emission to originate from the same mode, i.e. the Q-mode (Fig. 7). It refrained from decomposing the Q-mode modulation into further disjoint modes. In fact, a hint of Q-mode modulation is visible in the  $N_p$  time series (Figs. 6 and 7). However, it is fully explained as autoregressive behaviour with positive  $\phi_1$  and noise. Given our current modelling technique and available data, we conclude that the Q-mode modulation is longitude-stationary amplitude modulation and a separate phenomenon from mode-switching.

#### 4.4. Q-mode internal phase locking versus asynchronous mode-switching

Our data nicely demonstrate the phase-locked mode-switching between the pulsar's MP, PC, and IP profile components. The PC and MP switch fluence synchronously to each other (positively correlated), while both switch asynchronously (anti-correlated) to the IP (Fig. 14). This is a well known, but poorly understood phenomenon (Fowler & Wright 1982; Dyks et al. 2005). Additionally, we discovered that the MP and IP emission are phase-locked at a lower level during the pulsar's Q-mode (Fig. 11). This has not been reported before, as far as we know. Both the MP and IP exhibit the same amplitude modulation periodicity,  $P_3 = (41.7 \pm 0.9) P_1$ , and are positively correlated, meaning synchronous fluence modulation. Interestingly, the correlation behaviour within the Q-mode seems to be reversed compared with the overall mode-switching.

#### 4.5. Peculiar single-pulse phenomena

There are at least five peculiar single-pulse phenomena happening in PSR B1822–09: (1) extensive quasi-periodic microstructure in the PC, (2) PC activity within the Q-mode (mode mixing or instantaneous switches), (3) square-like almost null pulses, (4) extremely bright pulses, and (5) pulse intensity fading in after mode-switches. Only some of these have been described in the literature.

#### 4.6. Magnetar-like precursor component characteristics

PSR B1822–09’s PC component shows several emission characteristics reminiscent of radio-loud magnetars. It has an unusually flat spectral index (Fowler et al. 1981; Gil et al. 1994), a linear polarisation fraction close to 100 per cent (Manchester et al. 1980; Johnston & Kerr 2018), strong variability, and exhibits spiky emission with extremely narrow (0.2 – 0.4 ms) and intense quasi-periodic shot-like bursts, which often exceed the MP flux density per bin. In contrast, the MP behaves more like an ordinary radio pulsar pulse, except for the longitude-stationary amplitude around the MP’s leading profile hump. Thus, it seems that the pulsar combines both magnetar and canonical radio pulsar attributes, which is rarely seen in the known pulsar population.

## 5. Conclusions

PSR B1822–09 is an interesting pulsar that exhibits complex behaviour at the single-pulse level. We presented its single-pulse stacks and integrated profile at 650 MHz, investigated its mode-changing properties using a novel hidden Markov switching model, applied a fluctuation spectra analysis to the data, and discussed its single-pulse profile morphology. In the latter, we focused on five peculiar phenomena found in our data. We significantly added to the already extensive literature about this pulsar and confirmed several of its properties, while refuting others. While doing so, we introduced several new analysis techniques to the pulsar domain. This work demonstrates what is already possible with a small subset of the SUSPECT project data.

## 6. Data availability

The high-level data underlying this article will be shared on reasonable request to the corresponding author.

*Acknowledgements.* We thank Killian Lebreton for his contributions to this work as part of his Master’s degree project at the Université d’Orléans, the Nançay – Orléans pulsar group for helpful discussions, Yogesh Maan for clarifications about uGMRT data reduction, and the staff of the GMRT who have made these observations possible. We acknowledge the use of the Nançay Data Centre computing facility (CDN – Centre de Données de Nançay). The CDN is hosted by the Observatoire Radioastronomique de Nançay in partnership with Observatoire de Paris, Université d’Orléans, OSUC and the CNRS. The CDN is supported by the Région Centre Val de Loire, département du Cher. The GMRT is run by the National Centre for Radio Astrophysics of the Tata Institute of Fundamental Research. This work has been supported by ANR-20-CE31-0010.

## References

Akaike, H. 1974, *IEEE Transactions on Automatic Control*, 19, 716  
 Backer, D. C. 1970a, *Nature*, 228, 752  
 Backer, D. C. 1970b, *Nature*, 227, 692  
 Backer, D. C. 1970c, *Nature*, 228, 1297  
 Backer, D. C. 1970d, *Nature*, 228, 42  
 Backer, D. C. 1973, *ApJ*, 182, 245

Backus, I., Mitra, D., & Rankin, J. M. 2010, *MNRAS*, 404, 30  
 Basu, R., Mitra, D., & Melikidze, G. I. 2021, *ApJ*, 917, 48  
 Biggs, J. D. 1992, *ApJ*, 394, 574  
 Cao, S., Jiang, J., Dyks, J., et al. 2023, arXiv e-prints, arXiv:2312.11984  
 Cordes, J. M. 1978, *ApJ*, 222, 1006  
 Davies, J. G., Lyne, A. G., & Seiradakis, J. H. 1972, *Nature*, 240, 229  
 Dyks, J., Zhang, B., & Gil, J. 2005, *ApJ*, 626, L45  
 Edwards, R. T. & Stappers, B. W. 2002, *A&A*, 393, 733  
 Fowler, L. A. & Wright, G. A. E. 1982, *A&A*, 109, 279  
 Fowler, L. A., Wright, G. A. E., & Morris, D. 1981, *A&A*, 93, 54  
 Gil, J. A., Jessner, A., Kijak, J., et al. 1994, *A&A*, 282, 45  
 Hamilton, J. D. 1989, *Econometrica*, 57, 357  
 Hamilton, J. D. 2020, *Time series analysis* (Princeton university press)  
 Hankins, T. H. & Fowler, L. A. 1986, *ApJ*, 304, 256  
 Hermsen, W., Kuiper, L., Basu, R., et al. 2018, *MNRAS*, 480, 3655  
 Hermsen, W., Kuiper, L., Hessels, J. W. T., et al. 2017, *MNRAS*, 466, 1688  
 Hobbs, G. B., Edwards, R. T., & Manchester, R. N. 2006, *MNRAS*, 369, 655  
 Hotan, A. W., van Straten, W., & Manchester, R. N. 2004, *PASA*, 21, 302  
 Jankowski, F., Bailes, M., van Straten, W., et al. 2019, *MNRAS*, 484, 3691  
 Johnston, S. & Kerr, M. 2018, *MNRAS*, 474, 4629  
 Kramer, M., Lyne, A. G., O’Brien, J. T., Jordan, C. A., & Lorimer, D. R. 2006, *Science*, 312, 549  
 Latham, C., Mitra, D., & Rankin, J. 2012, *MNRAS*, 427, 180  
 Liu, J., Wang, H.-G., Shen, Z.-Q., et al. 2022, *ApJ*, 931, 103  
 Lorimer, D. R. 2011, *SIGPROC: Pulsar Signal Processing Programs*, *Astrophysics Source Code Library*, record ascl:1107.016  
 Lyne, A., Hobbs, G., Kramer, M., Stairs, I., & Stappers, B. 2010, *Science*, 329, 408  
 Lyne, A. G., Stappers, B. W., Freire, P. C. C., et al. 2017, *ApJ*, 834, 72  
 Maan, Y., van Leeuwen, J., & Vohl, D. 2021, *A&A*, 650, A80  
 Manchester, R. N., Hamilton, P. A., & McCulloch, P. M. 1980, *MNRAS*, 192, 153  
 Manchester, R. N., Hobbs, G. B., Teoh, A., & Hobbs, M. 2005, *AJ*, 129, 1993  
 Mandrou, P., Vedrenne, G., & Masnou, J. L. 1980, *Nature*, 287, 124  
 Morris, D., Graham, D. A., & Bartel, N. 1981, *MNRAS*, 194, 7  
 Pinkau, K. 1979, *Nature*, 277, 17  
 Prinz, T. & Becker, W. 2015, arXiv e-prints, arXiv:1511.07713  
 Rankin, J. M., Rodriguez, C., & Wright, G. A. E. 2006, *MNRAS*, 370, 673  
 Shabanova, T. V. 2007, *Ap&SS*, 308, 591  
 Smith, D. A., Abdollahi, S., Ajello, M., et al. 2023, *ApJ*, 958, 191  
 Song, X., Weltevrede, P., Szary, A., et al. 2023, *MNRAS*, 520, 4562  
 Stovall, K., Ray, P. S., Blythe, J., et al. 2015, *ApJ*, 808, 156  
 Suleymanova, S. A., Logvinenko, S. V., & Smirnova, T. V. 2012, *Astronomy Reports*, 56, 207  
 Szary, A., Zhang, B., Melikidze, G. I., Gil, J., & Xu, R.-X. 2014, *ApJ*, 784, 59  
 van Straten, W. & Bailes, M. 2011, *PASA*, 28, 1  
 Verbiest, J. P. W., Weisberg, J. M., Chael, A. A., Lee, K. J., & Lorimer, D. R. 2012, *ApJ*, 755, 39  
 Wahl, H. M., Orfeo, D. J., Rankin, J. M., & Weisberg, J. M. 2016, *MNRAS*, 461, 3740  
 Wang, N., Manchester, R. N., & Johnston, S. 2007, *MNRAS*, 377, 1383  
 Welch, P. D. 1967, *IEEE Trans. Audio & Electroacoust.*, 15, 70  
 Weltevrede, P. 2016, *A&A*, 590, A109  
 Weltevrede, P., Edwards, R. T., & Stappers, B. W. 2006, *A&A*, 445, 243  
 Yan, W. M., Manchester, R. N., Wang, N., et al. 2019, *MNRAS*, 485, 3241  
 Yao, J. M., Manchester, R. N., & Wang, N. 2017, *ApJ*, 835, 29  
 Yuan, J. P., Wang, N., Manchester, R. N., & Liu, Z. Y. 2010, *MNRAS*, 404, 289

## List of Objects

- ‘PSR B1822–09’ on page 2
- ‘PSR J1825–0935’ on page 2